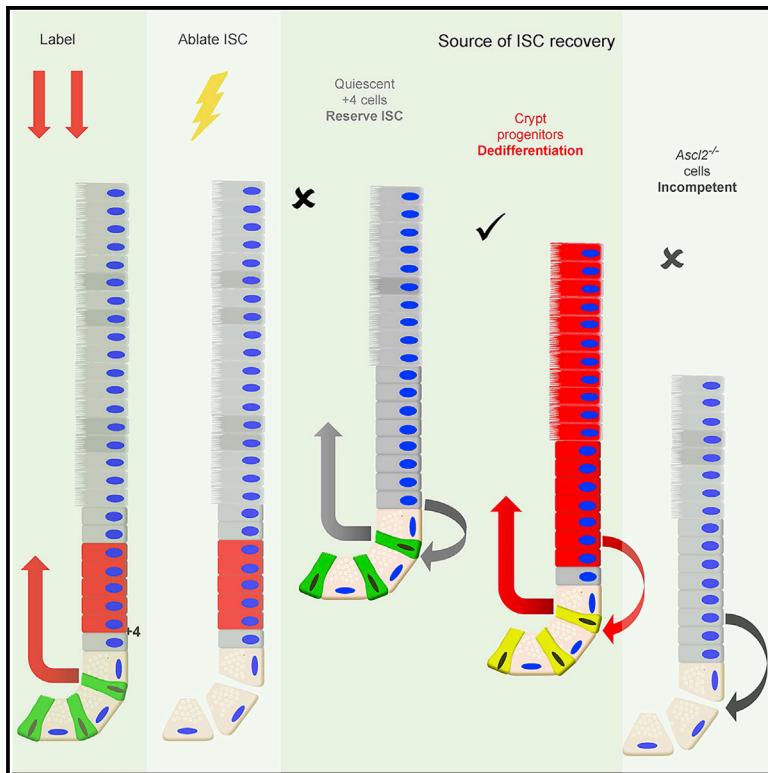# Cell Stem Cell

Ascl2-Dependent Cell Dedifferentiation Drives Regeneration of Ablated Intestinal Stem Cells

Graphical Abstract

Authors

Kazutaka Murata, Unmesh Jadhav, Shariq Madha, ..., Franziska Michor, Hans Clevers, Ramesh A. Shivdasani

Correspondence

ramesh_shivdasani@dfci.harvard.edu

In Brief

Quiescent reserve "+4 crypt cells" are thought to be a major source for recovery of ablated intestinal stem cells. Shivdasani et al. show instead that recovery occurs almost exclusively by dedifferentiation of recent stem cell progeny, which requires the transcription factor ASCL2 for this restorative potential.

Highlights

- Ablated intestinal stem cells (ISC) restore largely by crypt cell dedifferentiation

- ISC-restricted transcription factor ASCL2 is required for this adaptive regeneration

- Both absorptive and secretory lineages contribute to ISC restoration

- ASCL2-dependent IL11RA1 activity enhances ISC recovery from dedifferentiating cells

CellPress

Ascl2-Dependent Cell Dedifferentiation Drives Regeneration of Ablated Intestinal Stem Cells

Kazutaka Murata,[1,2] Unmesh Jadhav,[1,2] Shariq Madha,[1] Johan van Es,[3] Justin Dean,[4,5] Alessia Cavazza,[1,2] Kai Wucherpfennig,[6] Franziska Michor,[4,5] Hans Clevers,[3] and Ramesh A. Shivdasani[1,2,7,8,*]

[1]Department of Medical Oncology and Center for Functional Cancer Epigenetics, Dana-Farber Cancer Institute, Boston, MA 02215, USA
[2]Departments of Medicine, Brigham & Women's Hospital and Harvard Medical School, Boston, MA 02215, USA
[3]Hubrecht Institute, Royal Netherlands Academy of Arts and Sciences (KNAW) and University Medical Centre (UMC) Utrecht, 3584 CT Utrecht, the Netherlands
[4]Department of Cancer Data Sciences, Dana-Farber Cancer Institute, and Department of Biostatistics, Harvard T.H. Chan School of Public Health, Boston, MA 02215, USA
[5]Department of Stem Cell and Regenerative Biology, Harvard University, Cambridge, MA 02138, USA
[6]Department of Cancer Immunology, Dana-Farber Cancer Institute, Boston, MA 02215, USA
[7]Harvard Stem Cell Institute, Cambridge, MA 02138, USA
[8]Lead Contact
*Correspondence: ramesh_shivdasani@dfci.harvard.edu
https://doi.org/10.1016/j.stem.2019.12.011

SUMMARY

Ablation of LGR5^{+} intestinal stem cells (ISCs) is associated with rapid restoration of the ISC compartment. Different intestinal crypt populations dedifferentiate to provide new ISCs, but the transcriptional and signaling trajectories that guide this process are unclear, and a large body of work suggests that quiescent "reserve" ISCs contribute to regeneration. By timing the interval between LGR5^{+} lineage tracing and lethal injury, we show that ISC regeneration is explained nearly completely by dedifferentiation, with contributions from absorptive and secretory progenitors. The ISC-restricted transcription factor ASCL2 confers measurable competitive advantage to resting ISCs and is essential to restore the ISC compartment. Regenerating cells re-express *Ascl2* days before *Lgr5*, and single-cell RNA sequencing (scRNA-seq) analyses reveal transcriptional paths underlying dedifferentiation. ASCL2 target genes include the interleukin-11 (IL-11) receptor *Il11ra1*, and recombinant IL-11 enhances crypt cell regenerative potential. These findings reveal cell dedifferentiation as the principal means for ISC restoration and highlight an ASCL2-regulated signal that enables this adaptive response.

INTRODUCTION

LGR5[+] intestinal stem cells (ISCs) sustain small intestine and colonic epithelial self-renewal (Barker et al., 2007), but their ablation does not compromise epithelial integrity, because other crypt cells soon replenish the LGR5^{+} compartment (Tian et al., 2011). It remains controversial whether this homeostatic response reflects activation of a "reserve" pool of quiescent ISCs or occurs only by dedifferentiation of LGR5^{+} cells' recent

progeny (Bankaitis et al., 2018; Santos et al., 2018; Yousefi et al., 2017). The parameters and molecular basis of crypt cell plasticity are also largely unknown (de Sousa e Melo and de Sauvage, 2019).

Intestinal crypts and villi rapidly lose S-phase labels as a result of DNA replication and cell attrition. A central argument for "reserve" ISCs is that rare cells in crypt tier 4 retain S-phase tags for many days, signifying the putative stem cell hallmark of replicative quiescence (Potten, 1998). Cells expressing markers such as *Bmi1*, *Tert*, and *Hopx* also concentrate near tier 4 (Montgomery et al., 2011; Sangiorgi and Capecchi, 2008; Takeda et al., 2011) and LGR5^{+} cells restored after ISC loss originate in a *Bmi1^{+}* population (Tian et al., 2011), reinforcing the idea of dedicated "reserve" *Bmi1^{+}* ISCs. When label-retaining cells (LRCs) are followed for >3 weeks, however, S-phase tags shift into Paneth and enteroendocrine (EE) cells, indicating that LRCs are secretory (Sec) cell precursors (Buczacki et al., 2013). Moreover, *Bmi1^{hi}* and *Tert[+]* populations contain mainly EE cells (Jadhav et al., 2017; Yan et al., 2017), and *Bmi1* mRNA is expressed in many crypt (Itzkovitz et al., 2011; Muñoz et al., 2012) and even villus (Ayyaz et al., 2019; San Roman et al., 2015) cells. Therefore, LGR5^{+} cell recovery from a *Bmi1^{+}* origin could reflect diverse sources (Barker et al., 2012), including EE cells and possibly rare "reserve" ISCs. Indeed, the idea of "reserve" LRCs remains popular (Ayyaz et al., 2019; Chaves-Perez et al., 2019).

In response to LGR5^{+} cell deficits, both Sec and enterocyte (Ent) progenitors (Tetteh et al., 2016; van Es et al., 2012), and occasionally even mature Paneth cells (Jones et al., 2019; Schmitt et al., 2018; Yu et al., 2018), contribute to a replenished ISC pool. This facility is explained in part by the remarkably similar profiles of active histones in ISCs and villus Ent cells (Kim et al., 2014) and by the observation that areas of open chromatin specific to the Sec lineage reverse readily upon ISC damage (Jadhav et al., 2017); thus, chromatin barriers between crypt cell states are low or easily breached. Although crypt cells can dedifferentiate, it remains unclear (1) if they account for the bulk of ISC restoration, (2) which crypt cells harbor this latent potential, and (3) if homeostasis might reflect contributions from both

LGR5$^+$ cell derivatives and reserve ISCs. Here we report that nearly all regeneration after ISC injury occurs by ASCL2-dependent dedifferentiation of recent LGR5$^+$ cell progeny.

The basic-helix-loop-helix transcription factor (TF) gene *Ascl2*, a transcriptional target of Wnt signaling, is restricted to LGR5$^+$ basal crypt cells in mice (van der Flier et al., 2009) and humans (Jubb et al., 2006). *Ascl2* deletion by *Ah-Cre* first indicated its requirement for ISC survival *in vivo* (van der Flier et al., 2009), but *Ascl2$^{-/-}$* organoids later revealed only ~30% growth disadvantage, attributed in part to its co-regulation of Wnt-responsive genes (Schuijers et al., 2015). Using both the original and a new conditional mutant allele, we show that in the absence of ISC injury, ASCL2 confers a modest competitive advantage for cells to occupy the ISC niche. In contrast, ASCL2 is indispensable *in vivo* for crypt cell dedifferentiation after ISC injury. After ISC ablation, ectopic *Ascl2* expression in colonic crypts allowed us to detect and purify actively dedifferentiating cells. mRNA profiles of restorative populations and single cells lacked evidence for a favored +4 cell source and revealed dynamic transcriptional flux in colonocytes and goblet cells, each converging toward ISCs. Bona fide developmental genes and YAP/TAZ signaling were not appreciable elements of that flux. Coupled evaluation of mRNAs and ASCL2-bound promoters in regenerating cells revealed the interleukin-11 (IL-11) receptor gene *Il11ra1* as a transcriptional target, and organoid cultures demonstrated IL-11 activity in ISC regeneration. Together, these findings establish crypt cell dedifferentiation as the principal means to restore damaged ISCs and reveal one of likely several ASCL2-dependent enabling signals.

RESULTS

Following Ablation, ISCs Regenerate Exclusively from Daughter Crypt Cells

To identify the principal source of regenerated ISCs, we crossed *Lgr5$^{GFP-CreER(T2)}$* (*Lgr5$^{Gfp-Cre}$*) (Barker et al., 2007) and *R26R^{tdTom}* mice (all strains are listed in the Key Resources Table), then treated adult animals with tamoxifen (TAM), hence permanently labeling the progeny of Lgr5$^+$ ISCs. Accordingly, after an ISC-ablative dose of γ-irradiation (Metcalfe et al., 2014), ISCs restored from Lgr5$^+$ cells' recent progeny, and the resulting crypts, should emit red fluorescence. In contrast, on the basis of the independent origins and replicative quiescence of putative "reserve" ISCs (Li and Clevers, 2010), Lgr5$^+$ ISCs and the associated crypts arising from "reserve" ISCs will lack that signal (Figure 1A). The *Lgr5$^{GFP-Cre}$* allele is active in a fraction of intestinal crypts (Barker et al., 2007), and 24 h after radiation all crypts lacked GFP (Figure S1A), as expected. ISCs were restored within 6 days, when nearly every recovered crypt in small intestines and ~80% of colonic crypts housed tdTom$^+$ cells and GFP$^+$ ISCs (Figures 1B and 1C). Corroborating these rigorous counts of every GFP$^+$ crypt by microscopy, flow cytometry revealed tdTom in >99% of duodenal GFP$^+$ ISCs (Figure 1D). Thus, regenerated ISCs arise almost exclusively from their own recent progeny, with at best a small contribution from older cells. Because colonic epithelium turns over more slowly than the small intestine (Barker et al., 2007; Cheng and Bjerknes, 1985), the fraction of GFP$^+$tdTom$^-$ crypts in the recovered colon likely reflects inefficient labeling of ISC progeny before irradiation.

Dll1$^+$ intestinal Sec progenitors can restore ISCs damaged by γ-irradiation (van Es et al., 2012), and Ent progenitors contribute when ISCs expressing the *Diphtheria* toxin receptor (DTR) are ablated by exposure to *Diphtheria* toxin (DT) (Tetteh et al., 2016). Other studies confirm the role of Atoh1$^+$ Sec cells in low-level baseline ISC production, which increases upon epithelial injury (Ishibashi et al., 2018; Tomic et al., 2018), but recent work suggests that Sec cells may alone replenish damaged colonic ISCs (Castillo-Azofeifa et al., 2019). Therefore, we asked if each lineage can restore ISCs when the other is depleted and when injury is exquisitely targeted to ISCs: by treating *Lgr5$^{Dtr-GFP}$* mice (Tian et al., 2011) with DT (Figures 1E and 1F). We examined crypt cell dedifferentiation in *Atoh1$^{-/-}$* intestines, which lack all Sec cells (Shroyer et al., 2007), and in Ent-depleted *Rbpj$^{-/-}$* intestines (Kim et al., 2014), using *Villin-Cre$^{ER(T2)}$* mice (el Marjou et al., 2004) to delete *Atoh1* (Shroyer et al., 2007) or *Rbpj* (Han et al., 2002) in all intestinal epithelial cells. The experimental schemes differed because Sec, especially Paneth, cells take up to 4 weeks to disappear after *Atoh1* deletion, and mice withstand this loss far longer than they survive after *Rbpj* deletion. In both cases, however, we measured recovery by counting GFP$^+$ ISCs in crypts 3 days after the last of four doses of DT. Neither absence (Figure 1E) nor substantial enrichment (Figures 1F and S1B) of Sec cells appreciably impaired full recovery of duodenal or colonic ISCs. Modestly impaired ISC recovery in *Rbpj$^{-/-}$* colon reflects either the larger fraction of Sec progenitors normally present in this organ or the poor health of animals, which survive only a few days after *Rbpj* deletion (Kim et al., 2014). Together, these findings indicate that, at least when Sec or Ent cells are missing, the other type dedifferentiates efficiently after ISC ablation.

Limited Requirement for ISC-Restricted Transcription Factor ASCL2 in Resting ISC Functions

After ISC loss, dedifferentiating EE and goblet cell precursors extensively alter chromatin access and mRNA expression (Jadhav et al., 2017). Because these changes are especially marked and rapid at the *Ascl2* locus (Figure S1C), which was previously implicated in Lgr5$^+$ ISC survival (van der Flier et al., 2009), we generated a new mouse allele, *Ascl2^{Dfci}* (Key Resources Table), which replaces the native coding region with a floxed bicistronic cassette that encodes *mCherry* (mCh) and FLAG epitope-tagged ASCL2 (Figure S1D). This allele allows detection of ASCL2$^+$ cells by fluorescence microscopy or flow cytometry, precipitation of ASCL2 with FLAG antibody (Ab), and CRE-mediated gene deletion. mCh signals were confined to the bottoms of all crypts (Figure S1E), below tier 5 (Figure 2A), co-localizing precisely with GFP in *Lgr5$^{GFP-Cre}$* (Barker et al., 2007) and *Lgr5$^{Dtr-GFP}$* (Tian et al., 2011) mice (Figure 2B). *Ascl2^{Dfci}* mice thus demonstrate tight *Ascl2* restriction in Lgr5$^+$ ISCs and can be used to visualize this cell population, especially in the colon, where fluorescence was consistently higher than in small intestine ISCs (Figure S1F).

Ascl2$^{+/Dfci}$ mice were healthy and born in Mendelian proportions, but the targeted allele failed to transmit through the maternal germline, probably because the *Ascl2* locus is imprinted, and we could not achieve homozygosity. We therefore crossed the mice with another *Ascl2^{Fl}* strain, which transmits a floxed allele (whole-gene deletion, hereafter called *Ascl2^{Umc}*;
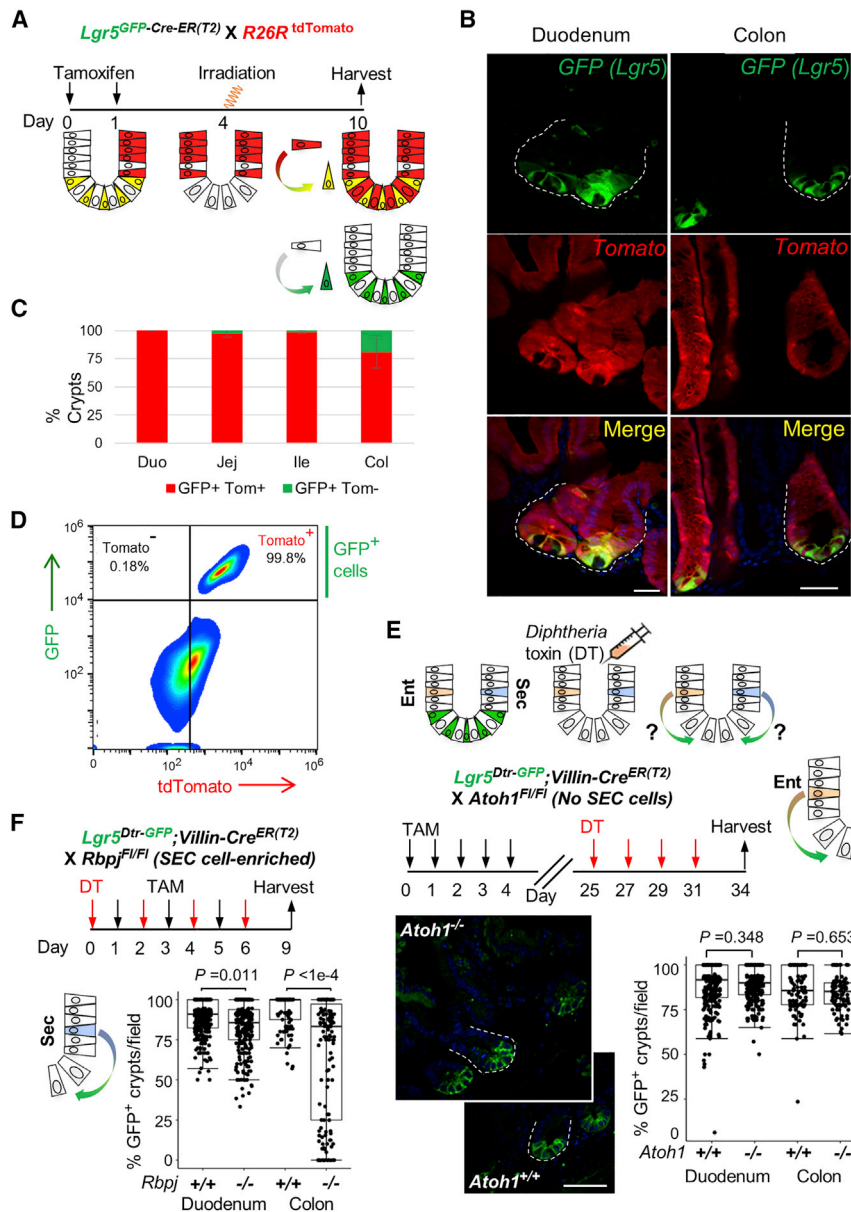
Figure 1. ISC Regeneration by Ent and Sec Progenitors

(A) Schema for ISC regeneration in $Lgr5^{GFP-Cre-ER(T2)}$; $R26R^{tdTom}$ mice. Lgr5$^+$ ISCs were ablated by γ-irradiation 4 days after induction of Cre to track tdTom$^+$ progeny 6 days thereafter. If ISCs regenerate from those progeny, then freshly restored GFP$^+$ ISCs will carry the tdTom label. If ISCs are restored from a separate reserve pool, those ISCs will express GFP but not tdTom.

(B and C) Representative micrographs (B) and quantitation (C) of crypts containing restored tdTom$^+$ and tdTom$^-$GFP$^+$ ISCs in the duodenum and colon 6 days after γ-irradiation. Scale bars, 50 μm. Bar graphs represent the tdTom$^+$ fraction (mean ± SD) in all (hundreds in each of n = 5 mice) GFP$^+$ crypts.

(D) Two-color (GFP and tdTom) flow cytometry of duodenal crypt cells isolated from TAM-treated $Lgr5^{GFP-Cre}$;$R26R^{tdTom}$ mice 6 days after γ-irradiation (n = 2 animals). tdTom$^+$ cells represent GFP$^+$ ISCs (>99% express tdTom) and their labeled GFP$^-$ progeny.

(E and F) Experimental schemes and results of ISC restoration in DT-treated $Lgr5^{Dtr-GFP}$ mice by Ent cells when the Sec lineage is absent ($Atoh1^{-/-}$, E) or by Sec cells when the Ent lineage is depleted ($Rbpj^{-/-}$, F). Tamoxifen (TAM) was administered to delete genes, and DT was given to ablate ISCs. Every GFP$^+$ crypt was counted on the indicated days in $Atoh1^{-/-}$ (n = 6) or $Rbpj^{-/-}$ (n = 4) intestines and equal numbers of controls. Within the plots, boxes demarcate quartiles 1 and 3, bars represent median values, whiskers represent 1.5 times the inter-quartile range, and differences were assessed using Student's t test. Dotted white lines in representative micrographs outline selected crypts. Scale bars, 50 μm.

See also Figure S1.

ostensibly intact ISC activity (Figure S2C), indicating that ASCL2 is dispensable for resting ISC function.

Although ISC survival is compromised in Ah-Cre;$Ascl2^{Fl/Fl}$ mice (van der Flier et al., 2009), our findings agree with a subsequent study showing modestly reduced ability of $Villin$-Cre;$Ascl2^{Fl/Fl}$ ISCs to form organoids (Schuijers et al., 2015). This difference may reflect unknown effects of β-naphthoflavone-mediated gene deletion in Ah-Cre mice; alternatively, $Ascl2$ deletion may have been inefficient in our experiments. To exclude the latter possibility, note that recombination of $Ascl2^{Dfci}$ deletes coding exons as well as mCh (Figure S1D) and that PCR can discern parental from CRE-excised alleles (Figure S1H). mCh signals were substantially reduced after TAM exposure on the $Villin$-Cre background (Figure S2D), and both mCh$^+$GFP$^+$ ISCs (Figure 2F) and $Ascl2$ transcripts (Figure S2E) were much reduced on the $Lgr5^{Gfp-Cre}$ background. Genotyping confirmed significant recombination of targeted $Ascl2$ alleles (Figure S2F). Moreover, $Ascl2^{-/-}$ ISCs purified by GFP flow cytometry differed from $Ascl2$-proficient ISCs, purified by mCh flow cytometry, in expression of ∼3,500 mRNAs

Figures S1G and S1H) through both sexes (van der Flier et al., 2009), to derive $Ascl2^{Dfci/Umc}$ compound heterozygotes. Additional crosses allowed us to study consequences of ASCL2 loss throughout the intestinal epithelium (with $Villin$-Cre^{ER}) or from some crypts, starting in Lgr5$^+$ ISCs (with $Lgr5^{GFP-Cre}$). After activation of $Villin$-Cre^{ER} with TAM, both $Ascl2^{Dfci/Umc}$ and $Ascl2^{Umc/Umc}$ mice displayed no signs of malnutrition or illness, and intestinal histology was overtly normal (Figure S2A). Immunostains for Ki67 and cleaved caspase-3 revealed intact crypt cell proliferation (Figure 2C) and absence of appreciable apoptosis (Figure S2B). On the $Lgr5^{GFP-Cre}$ background, TAM-treated $Ascl2$-null (mCh$^-$GFP$^+$) and adjacent $Ascl2$-proficient (mCh$^+$GFP$^-$) crypts carried essentially similar ISC numbers (Figure 2D), a finding confirmed by GFP flow cytometry (Figure 2E). Moreover, lineage tracing by the $R26R^{Tom}$ reporter revealed
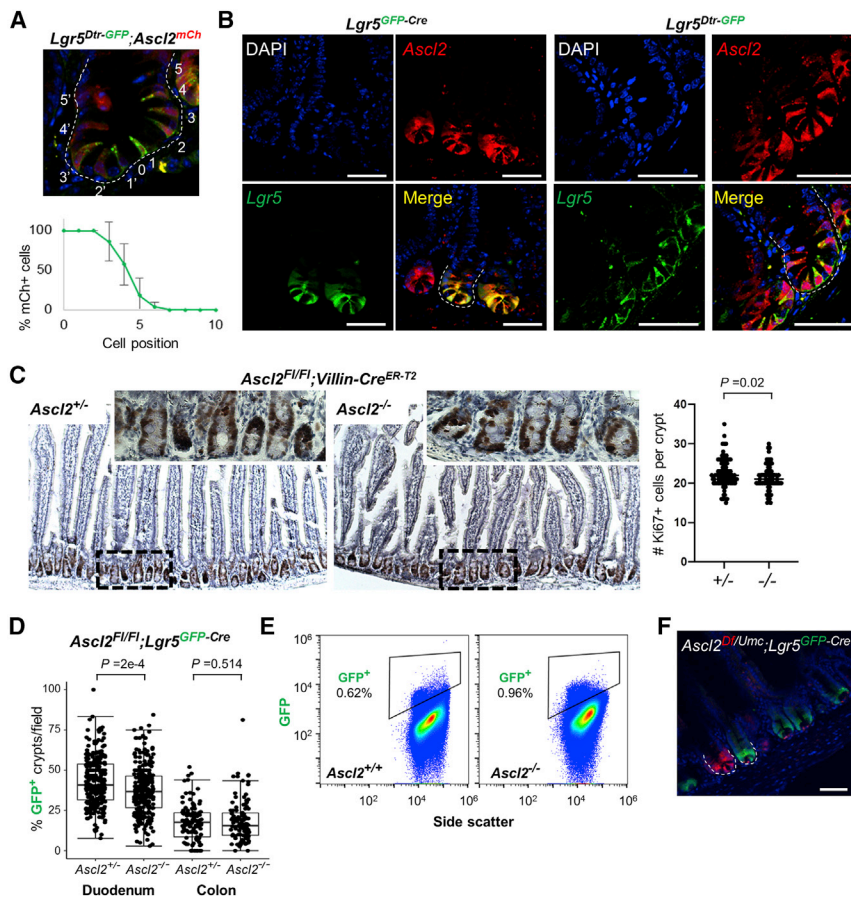
Figure 2. *Ascl2* Expression and Perturbation

(A) mCh[+] cell positions in *Ascl2*[Dfci] mouse intestines relative to the bottom of colonic crypts (tier 0; positions 1 and 1′, 2 and 2′, etc., correspond to higher tiers). Results are quantified below as mean ± SD (n = 4 mice).

(B) Confocal micrographs of mCh and GFP co-localization in the duodenum and colon of strains with mosaic (*Lgr5*[GFP-Cre]) and non-mosaic (*Lgr5*[Dtr-GFP]) GFP[+] ISCs. Results represent findings in at least five mice of each genotype. Scale bars, 50 μm. Dotted white lines outline single crypts.

(C) Duodenal crypt cell proliferation was largely intact after *Ascl2* deletion by *Villin-Cre*[ER-T2] (n = 3 mice of each genotype).

(D) Counts of all GFP[+] crypts in every microscopic field in *Ascl2*[+/Fl] and *Ascl2*[Fl/Fl] intestines (n = 5 mice each) on the *Lgr5*[GFP-Cre] background, 7 days after the first TAM dose. Differences in (C) and (D) were assessed using Student's t test.

(E) Flow cytometry confirmed persistence of duodenal GFP[+] ISCs in *Lgr5*[GFP-Cre];*Ascl2*[Fl/Fl] mice 7 days after TAM treatment. Data are shown for one pair from n = 2 mice of each genotype.

(F) In Cre-activated crypts, *Lgr*[GFP-Cre];*Ascl2*[Fl/Fl] mice lacked mCh expression, which was readily evident in neighboring Cre[−] (GFP[−]) crypts. Dashes outline single crypts; scale bar, 50 μm.

See also Figures S1 and S2.

(>2-fold, p_{adj} < 0.01; Figure S2G; Table S1), as expected with global absence of a functional TF. Escape from recombination is therefore small and cannot account for largely intact ISC function days after CRE activation.

ASCL2 Requirements in Neutral ISC Drift and in ISC Recovery after Injury

Ascl2^{−/−} ISCs could, however, be disadvantaged in prolonged competition with the minority of cells lacking biallelic gene deletion. Lgr5^{+} ISCs divide symmetrically, with each crypt becoming monoclonal by neutral drift over ~30 days (Lopez-Garcia et al., 2010; Snippert et al., 2010), but cells with a selective advantage prevail over time (Snippert et al., 2014; Vermeulen et al., 2013). Indeed, although GFP[+] (Cre[+]) crypts in *Lgr5*[Cre];*Ascl2*[Fl/Fl]; *R26R*[tdTom] mice first expressed tdTom uniformly after CRE activation, progressively larger fractions of these crypts lacked tdTom 1 and 4 months later (Figure 3A), implying replacement of *Ascl2*-null cells by ISCs with one or both *Ascl2* copies intact. Soon after TAM treatment, unrecombined tdTom^{−} cells were difficult to detect by microscopy, but DNA from GFP[+] duodenal ISCs revealed their presence at 5 days, and DNA at 1 month carried similar proportions of parental and recombined *Ascl2* alleles (Figure 3B). Even at 4 months, rare GFP[+] crypts housed both tdTom[+] and tdTom^{−} cells (Figure 3C), which implies ongoing drift and prolonged delay of monoclonality.

To estimate the selective *Ascl2*^{−/−} ISC disadvantage quantitatively, two-dimensional (2D) tissue sections did not accurately define cell ratios in the rare mixed crypts or the ISC fraction that escaped gene recombination. Instead we used the predominantly tdTom[+] and tdTom[−] crypt fractions in mice 28 (n = 2) and 112 (n = 5) days after *Ascl2* excision (Figure 3A) and adapted a previous (Lopez-Garcia et al., 2010) population genetics model of ISC dynamics (Figure 3D; STAR Methods). We considered starting ISC numbers (N) of 10–14 (Snippert et al., 2010), wild-type (WT) replication rates (λ_{WT}) of 0.5/day for duodenal and 0.25/day for colonic ISCs (Snippert et al., 2014), and variable numbers of cells rendered *Ascl2* null (M), where M/N > 0.7. We modeled possible *Ascl2*^{−/−} ISC replication rates (λ_{Mut}) by optimizing λ_{Mut} values over 1,000 simulations to minimize the squared distance between predicted and observed tdTom[+] (presumed Mut) and tdTom[−] (WT) crypt counts (e.g., Figures S3A and S3B). This model recapitulated the data and estimated relative *Ascl2*^{−/−} ISC fitness, $\lambda_{Mut}/\lambda_{WT}$, as ~0.5–0.75 in the duodenum and ~0.33–0.67 in the colon (Figures 3E and S3C). These estimates were robust over a wide range of parameters, largely insensitive to different ratios of M/N when N > 10, to a different duodenal λ_{WT} of 0.3 (Kozar et al., 2013), and whether simulations were fitted to mean or median 112-day crypt counts. The wide range of estimates resulted mainly from uncertainty about the fraction of *Ascl2*^{−/−} ISC (M/N), as expected, but very small changes in λ_{Mut} moved trajectories across the range of observed 112-day crypt counts, lending confidence in the range of values. Refinement of these provisional estimates will require additional animals, time points, and confident determination of values for M.

To determine whether ASCL2 is necessary to restore damaged ISCs, we first treated *Ascl2*[Umc/Umc];*Lgr5*[GFP-Cre] mice
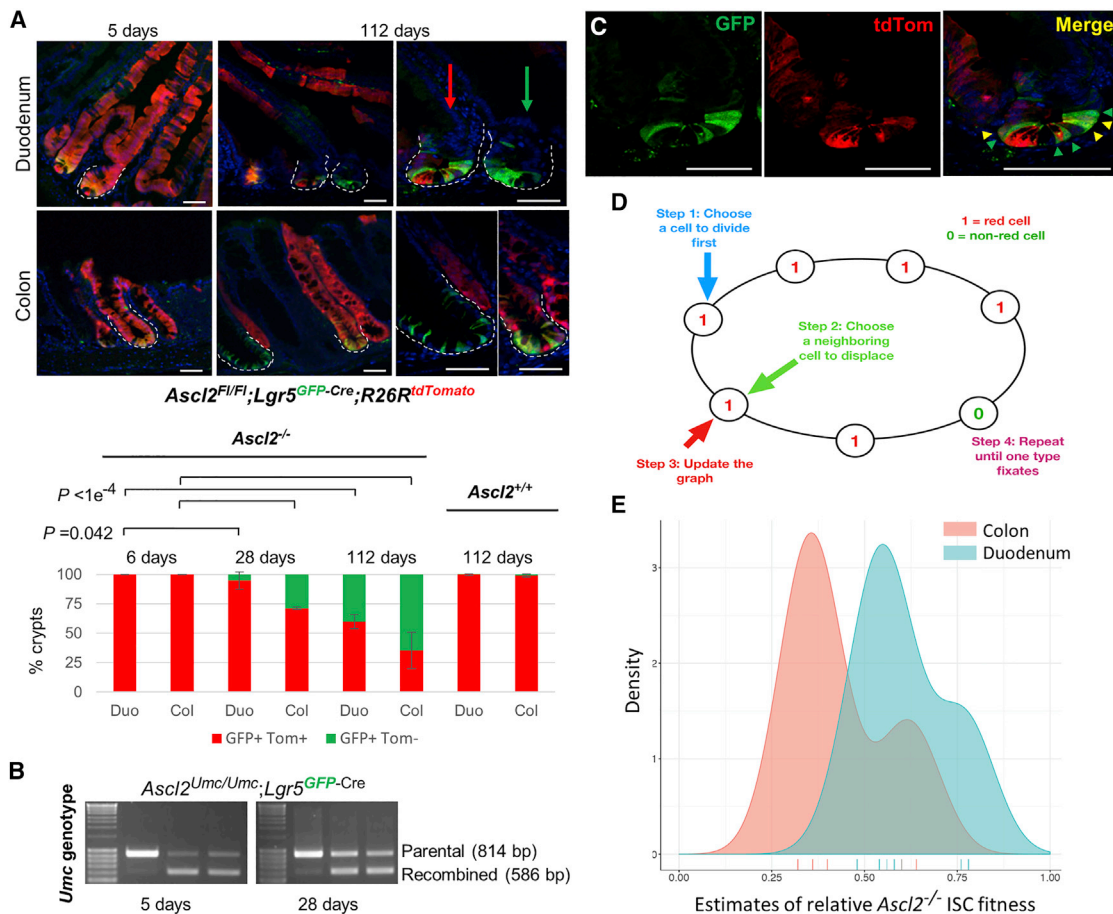
Figure 3. Reduced Fitness of *Ascl2*^{−/−} ISCs

(A) Early (5 days) and late (28 and 112 days) crypt composition after *Ascl2* deletion in *Lgr5*^{GFP-Cre};*R26R*^{tdTom} intestines. All GFP⁺ crypts on this mosaic background showed tdTom expression 5 days after the first dose of TAM, but the proportion of tdTom⁺ GFP⁺ crypts (red arrow) was reduced by 28 days (n = 2 animals) and substantially so by 112 days (n = 5 mice), when large fractions of duodenal and colonic GFP⁺ ISCs lacked tdTom (green arrow). Bar graphs depict mean crypt counts ± SD, and differences were evaluated using Student's t test. Thus, Lgr5⁺ cells that escaped *Ascl2* and *R26R* recombination (tdTom⁻) are selected over *Ascl2*-null (tdTom⁺) ISCs. Scale bars, 50 μm.

(B) Genotyping of GFP⁺ ISCs purified using flow cytometry 5 and 28 days after TAM treatment shows the presence of recombined (*Ascl2*-null) and parental (unrecombined, "escaper") alleles. The genotyping strategy is shown in Figures S1G and S1H.

(C) High-magnification micrographs showing the presence of tdTom⁻ (green arrowheads) and tdTom⁺ (yellow arrowheads) GFP⁺ ISCs in the same crypt. Such mixed crypts were rare (<15 per animal). tdTom⁺GFP⁻ cells are Paneth cells arising from tdTom⁺ ISCs that previously contributed to this representative crypt.

(D) Population genetics model for ISC dynamics (see STAR Methods). N number of ISCs are arranged on the cycle graph, representing crypts that contain infrequent tdTom⁻ "escaper" ISCs (0, WT) amid mostly recombined tdTom⁺ ISCs (1, *Ascl2*^{−/−}). During each time step of the stochastic model, we first sample an exponential waiting time for each ISC with rates λ_{WT} and λ_{Mut} for WT and mutant ISCs, respectively. The smallest waiting time defines which cell divides first. Thereafter, one resulting daughter takes the parent's spot, while the other usurps one of the two neighboring cells, each with probability 0.5. This cycle repeats over many cell divisions until crypts carry predominantly tdTom⁺ or tdTom⁻ ISCs (i.e., fixation), which was evident in mice examined 28 and 112 days after gene excision (A).

(E) Density plot of estimated *Ascl2*^{−/−} fitness (λ_{Mut}) values relative to WT duodenal or colonic ISCs (λ_{WT}), determined using simulations for different parameter regimes (see Figure S3C).

See also Figures S1 and S3.

with TAM to delete *Ascl2*, followed by 10 Gy γ-irradiation to ablate ISCs. Whereas GFP⁺ ISCs were quickly restored in control intestines, absence of ASCL2 prevented this recovery, and animals succumbed to the radiation injury (Figure 4A). Second, after using DT to kill ISCs in *Ascl2*^{Umc/Umc};*Lgr5*^{Dtr-GFP};*Villin-Cre*^{ER(T2)} mice, we gave TAM to activate CRE and delete *Ascl2* (Figure 4B). Again, whereas GFP⁺ ISCs were restored within 5 days in control animals, *Ascl2*-null intestines failed to recover in that period, and flow cytometry confirmed paucity of

GFP⁺ cells (Figure 4B). Mutant mice became progressively moribund over the next 3 days, and at euthanasia their intestines showed a persistent Lgr5⁺ ISC deficit (Figure 4C), tissue dysmorphology (Figure 4D), and reduced crypt cell proliferation (Figure S4A). Whether ISCs were ablated by irradiation or DT treatment, *Ascl2*^{−/−} crypts failed to revive in all intestinal regions (Figures S4B and S4C). Thus, unlike the subtle role in physiologic neutral drift, ASCL2 is essential for ISC recovery after lethal damage.
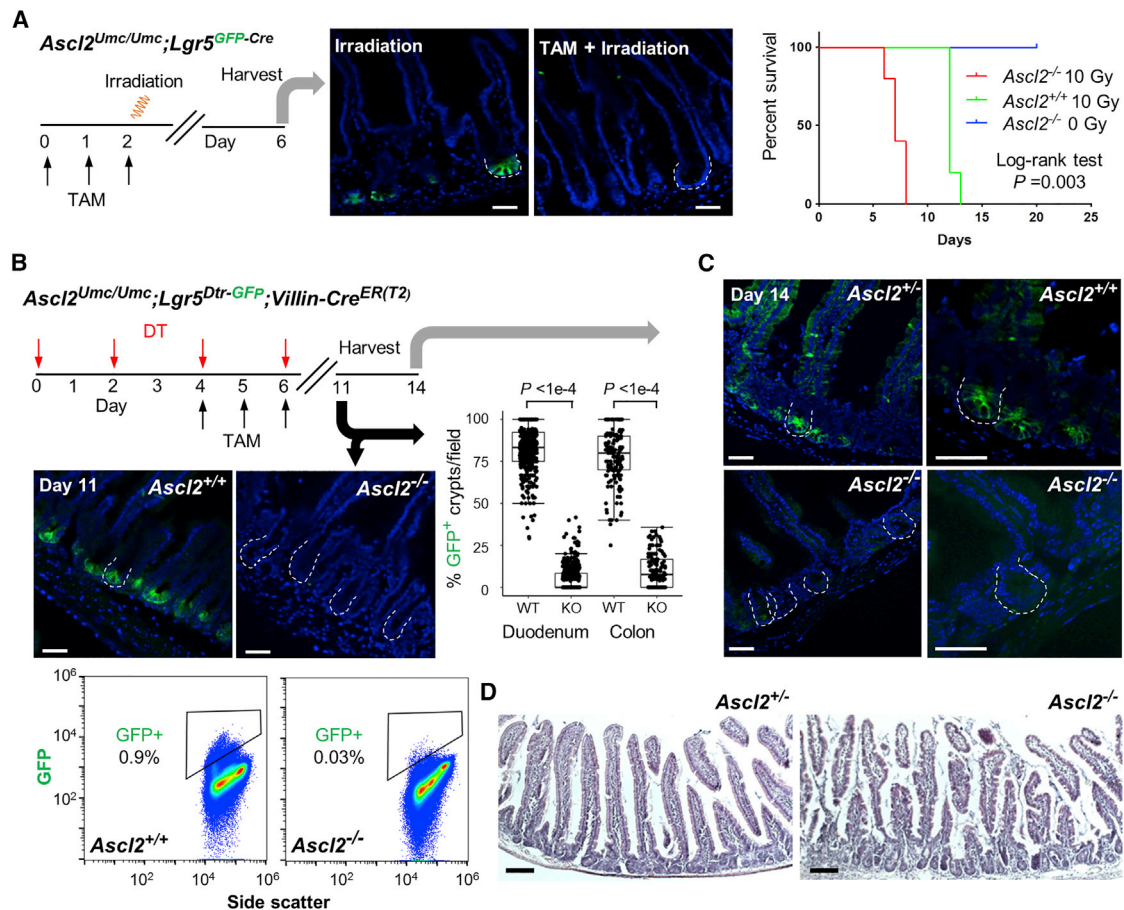
Figure 4. Ascl2 Requirement in ISC Restoration after Injury

(A) Test of *Ascl2* requirements in ISC regeneration after 10 Gy γ-irradiation of *Lgr5^GFP-Cre* mice. GFP+ ISCs failed to regenerate in the absence of ASCL2. Graph depicts survival of unirradiated mice with *Ascl2^−/−* intestines and mice with *Ascl2^+/+* or *Ascl2^−/−* intestines after irradiation (n = 5 animals per cohort). Differences were assessed using the log rank test.

(B) *Ascl2* requirement for ISC restoration after *Lgr5^Dtr-GFP* mice were treated with DT. In mice harvested on day 11 of the study, all GFP+ crypts were counted in every microscopic field in experimental (*Ascl2^−/−*) and two groups of control (*Ascl2^+/+* and no DT treatment) intestines (n = 4 mice per cohort) harvested on day 11. Boxes, quartiles 1 and 3; bars, median values; whiskers, 1.5 times the inter-quartile range. Differences were assessed using Student's t test. Fluorescence micrographs representing four experimental pairs and flow cytometry data representing one of n = 2 experimental pairs demonstrate the paucity of duodenal GFP+ ISCs in *Ascl2^−/−* intestines.

(C and D) Representative fluorescence micrographs (C; dotted white lines outline selected crypts) and histology (D; H&E stain) from intestines harvested from two mice on day 14, showing absence of GFP+ crypt base cells and distorted tissue morphology, which was patchy. Scale bars, 50 μm.

See also Figure S4.

Extensive Ascl2 Activation in Crypt Cells before Complete Dedifferentiation into ISCs

As the latter findings suggest that *Ascl2* may act in crypt cell dedifferentiation, we examined *Ascl2^+/Dfci*;*Lgr5^Dtr-GFP* intestinal crypts before and after treating mice with DT to eliminate mCh+ ISCs (Figure 5A). Abundant mCh+ cells now appeared well above crypt tier 5; over the next 2 days they progressed toward the crypt base (quantified in Figure 5B) and eventually expressed GFP (i.e., *Lgr5*) (Figure 5A), similar to resting ISCs. Thus, progenitor cells that otherwise lack *Ascl2* (see Figures 2A and 2B) activate expression as they dedifferentiate. These "upper" mCh+ cells, readily seen in the regenerating colon (Figures 5A and 5B), were difficult to visualize in the small intestine, where *Ascl2* RNA levels in resting ISCs are lower than those in the colon (Figure S1F). Flow cytometry of DT-exposed colonic

crypt cells confirmed a sizable mCh+GFP− cell population, distinct from native resting mCh+GFP+ ISCs (Figures 5C, S5A, and S5B), allowing us to isolate both populations. When cultured in medium containing Wnt, epidermal growth factor, Rspo, and Notch ligand (WERN), mCh+GFP− cells from DT-exposed crypts generated typical colonic organoids (Sasaki et al., 2016; Sato et al., 2009), far in excess of similar structures produced by equal numbers of native mCh+GFP+ colonic ISCs (Figure 5D). "Upper" cell-derived organoids had an epithelial lining and could be passaged successfully *in vitro* (Figure S5C), indicating that they contain self-renewing ISCs. In contrast, mCh−GFP− cells from DT-treated mice yielded few small spheroids, possibly reflecting ISC potential in some crypt cells that do not yet express *Ascl2*/mCh, and those from untreated mice yielded none (Figure 5D). These data reveal robust *Ascl2* inactivation in
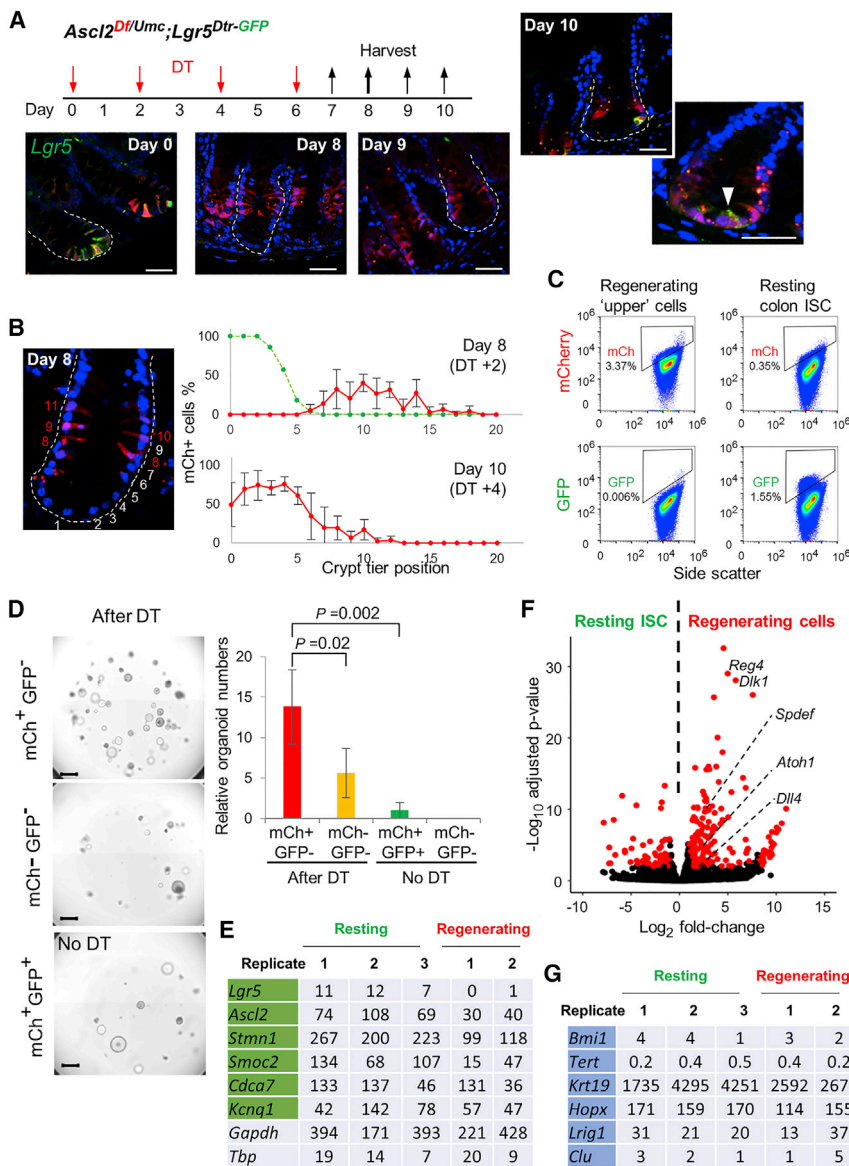
Figure 5. *Ascl2* Expression in Colonic Non-stem Crypt Cells after ISC Ablation

(A) *Lgr5*[Dtr-GFP] ISCs were ablated by administering DT, followed by colon harvests on days 7, 8, 9, and 10. mCh first appeared on day 8 in cells located well above the ISC zone, in positions never occupied by mCh^{+} cells in the absence of ISC injury (see Figures 2A and 2B). Each subsequent day, mCh^{+} cells appeared in positions closer to the crypt base, and by day 10, many of these cells acquired GFP expression (arrowhead in inset micrograph). Scale bars, 50 μm.

(B) Illustrative tier positions and manual counts of mCh^{+} cells (red) relative to the crypt bottom on days 8 (n = 5 mice) and 10 (n = 3 mice). The green line (from Figure 2A) depicts mCh[+] cell positions in untreated animals (n = 4 mice).

(C) Flow cytometry confirmed that mCh^{+} crypt cells on day 8 lack GFP and give higher mCh signals than resting ISCs (additional examples and comparative statistics shown in Figure S5B).

(D) Organoid formation *in vitro* by single GFP^{−} cells (mCh[+] or mCh[−]) captured using flow cytometry from the same animals (n = 3) on day 8. mCh^{+} cells formed organoids more efficiently than mCh^{−} cells or native stem cells (mCh[+]GFP[+] from uninjured mice). Each image is a composite of multiple overlaid photomicrographs. Scale bars, 1 mm. Relative organoid numbers (yellow, red bars) are expressed in relation to those cultured from resting ISCs (green bar).

(E–G) Differential gene expression in uninjured (resting) colonic ISCs and regenerating day 8 mCh[+] "upper" crypt cells, determined by DEseq2 analysis of RNA-seq data. Overall differences (>log$_2$ 1.5-fold, q < 0.05) were limited to 316 genes, most of which increased in regenerating cells (F). Reads per kilobase per million sequence tags (RPKM) values from replicate samples show that the regenerating "upper" cell population lacked *Lgr5* but expressed many ISC-specific mRNAs (E) and that markers attributed to +4 "reserve' ISCs were absent or equally expressed in resting and regenerating colonic ISCs (G). *Gapdh*, *Tbp* confirm proper normalization of RNA-seq data.

See also Figure S5 and Tables S1 and S2.

a large fraction of colonic crypt cells destined to dedifferentiate into ISCs.

To study ASCL2-dependent crypt dedifferentiation, we purified regenerating mCh[+] (Ascl2^{+}) "upper" cells using flow cytometry and used RNA sequencing (RNA-seq) to compare their bulk RNA profiles with those of uninjured resting ISCs (Table S1). Among 485 genes specific to Lgr5^{+} ISCs in the small intestine (Muñoz et al., 2012), 176 genes are expressed in resting colonic ISCs at appreciable levels (>10 reads per kilobase per million sequence tags [RPKM]), and 401 genes express at any level (>1 RPKM; Figure S5D). Among these ISC-restricted mRNAs, 149 were appreciably present (>10 RPKM) and 365 were expressed (>1 RPKM) in upper mCh^{+} cells (Table S2), including *Cdca7* and *Smoc2* (Figure 5E). As a population, upper cells differed from resting ISCs in the levels of only 316 mRNAs (q < 0.01; Figure 5F; Table S1), implying that although regenerating Ascl2^{+} cells lack GFP protein (Figures S5A and S5B) or *Lgr5*

mRNA (Figure 5E), they are likely well on a path to acquire ISC features. Upper cells were enriched for Sec but not for +4 cell markers (Figures 5F and 5G) and did not express mRNA (Figure 5G) or protein (Figure S5E) of the "revival" ISC marker Clu (Ayyaz et al., 2019).

"Enterospheres" expanded *in vitro* from crypts late in mouse gestation express many RNAs different from those in adult organoids (Fordham et al., 2013; Mustata et al., 2013). In some forms of ISC injury, dedifferentiating adult crypt cells are reported to recapitulate this transcriptional program, represented by *Ly6a/Sca1* and triggered in part by YAP/TAZ signaling (Nusse et al., 2018; Yui et al., 2018). To test this general idea in mCh[+] colonic "upper" cells induced upon DT ablation of ISCs, we extended an approach originally applied to mouse fetal small bowel endoderm (Banerjee et al., 2018) to isolate colonic EPCAM^{+} cells at embryonic days (E) 11, 12, 14, and 16. Among the 6,865 fetal transcripts that are reduced or absent in the

adult epithelium, mCh⁺ "upper" cells reproducibly expressed at most 183 genes (2.67%; Figure S5F). Enterosphere-specific RNAs overlap minimally with these genes and were expressed comparably in resting and regenerating ISCs (Figure S5G). Key intestinal YAP/TAZ signature genes (Gregorieff et al., 2015) also were not enriched in "upper" cells (Figure S5H), whereas Sec marker genes (Figure 5F) hinted that the population may carry Sec or multipotent progenitors.

Transcriptional Features and Trajectories of Crypt Cell Dedifferentiation

To resolve the mCh⁺ "upper" population, we used 10X Genomics single-cell RNA sequencing (scRNA-seq) to study single cells collected 2 days after the last DT dose (day 8 in the experimental scheme; Figure 5A). After excluding cells with low information content or a high fraction of mitochondrial RNAs (Figure S6A; STAR Methods), 3,254 cells were informative. Individual cells expressed *Ascl2* but little to no *Lgr5* mRNA (Figure 6A), consistent with mCh⁺GFP⁻ fluorescence (Figures S5A and S5B). ISC-restricted genes such as *Cdca7* and *Smoc2* (Table S2) further delineated distinct ISC-like cells (Figure 6A). Proliferative activity was largely confined to this population, while +4 cell markers were absent (e.g., *Clu*) or expressed broadly (e.g., *Bmi1*) (Figure 6B). Projection of cell-specific markers on a uniform manifold approximation and projection (UMAP) plot identified *Fabp2⁺ Car1⁺* colonocytes, abundant *Muc2⁺ Tff3⁺* goblet cells (Figure 6C), and a tiny fraction of *Chga⁺ Pyy⁺* EE cells (Figure S6B). Notably, 556 cells expressed appreciable levels of ISC genes as well as colonocyte or goblet cell markers (Figure 6D), implying that they represent a bona fide transition along a spectrum of mature and dedifferentiated states. Within that spectrum, genes from enterosphere/fetal (Fordham et al., 2013; Mustata et al., 2013) and YAP/TAZ signaling (Gregorieff et al., 2015; Yui et al., 2018) modules, including genes common to two (*Ly6d*) or all three (*Ly6c1* and *Ly6a/Sca1*) modules, did not concentrate in the transitional cells or show a consistent pattern; individual transcripts were largely absent or broadly expressed (Figure S6C).

To derive pseudotime trajectories on the basis of cell-to-cell differences in RNA expression, we used the Monocle algorithm (Trapnell et al., 2014), designating high expression of ISC markers as the cellular endpoint. This unsupervised approach identified a continuum of cell states, with abundant goblet cells and fewer colonocytes showing distinct trajectories (Figure 6E). Positioning of transitional cells and their corresponding mature precursors along the pseudotime axis highlighted the distinct properties. Colonocyte markers declined more rapidly in pseudotime than goblet cell markers; conversely, ISC markers appeared more gradually in dedifferentiating goblet cells than in colonocytes (Figure 6F). These data reveal both cell types as sources of regenerating colonic ISCs but do not distinguish whether goblet cells are the principal source, as proposed (Castillo-Azofeifa et al., 2019), or were captured more readily than colonocytes.

ASCL2 Target Genes Such as Il11ra1 Facilitate ISC Regeneration

To identify transcriptional targets of ectopic ASCL2 in regenerating mCh⁺ "upper" cells, we used the 3xFLAG epitope in ASCL2^DFCI (Figure S1D) to precipitate TF-bound genomic regions and identified 4,943 binding sites (Table S3). Because ISC restoration likely depends on multiple target genes and transcriptional target assignment to distant enhancers is inherently ambiguous, we focused on genes with promoter binding (n = 3,530) and altered expression in mCh⁺ crypt cells (n = 316). Most mRNA changes were gains (Figure 5F) and correlated with higher ASCL2 binding at promoters in "upper" cells than in resting ISCs (Figure 7A). Four candidate target genes encode cell surface receptors that we could assess in functional assays: *Fgf18* and *Nov*, which act respectively in fibroblast growth factor and Notch signaling; the Wnt receptor *Fzd9*; and the IL-11 receptor gene *Il11ra1* (Figures 7A and S7A). Neither FZD9 Ab nor recombinant (r) FGF18 or rNOV affected organoid formation by mCh⁺ "upper" crypt cells (Figure S7B), though we are unsure if rNOV is active *in vitro* or if FZD9 Ab neutralizes the receptor).

Il11ra1 is a noteworthy candidate because IL-11 protects animals from various forms of ISC ablation (Du et al., 1994; Liu et al., 1996; Potten, 1996). *Il11ra1* transcripts were significantly increased in every bulk isolate of mCh⁺ "upper" cells, compared with resting colonic Lgr5⁺ ISC (Figure 7B) and well represented in single-cell RNA (scRNA) analysis of regenerating ISCs, including transitional cells and especially in the goblet cell fraction (Figure 7C). Flow cytometry for surface IL11RA1 revealed a small fraction of IL11RA⁺ "upper" mCh⁺ cells, compared with none in resting mCh⁺ ISCs (Figure S7C). IL-11 signals transduce via STAT3 (Jenkins et al., 2007), and we detected phosphorylated STAT3 in rare "upper" cells, but never in the absence of crypt ablation (Figure 7D). Importantly, rIL-11 had a reproducible, dose-dependent effect in augmenting organoid formation (Figure 7E), which did not occur with other targeted perturbations (Figure S7B). This augmentation occurred only in upper cell, not in resting ISC cultures (Figure 7E), and organoids enhanced in response to IL-11 could be passaged serially (Figures 7F and S7D), indicating that they contain colonic ISCs. Although other signals likely also contribute, these findings collectively implicate *Il11ra1* as one functional target of ASCL2 control in ISC regeneration.

DISCUSSION

Both principal cell types derived from Lgr5⁺ ISCs (Tetteh et al., 2016; van Es et al., 2012) and even rare Paneth cells (Jones et al., 2019; Schmitt et al., 2018; Yu et al., 2018) help restore crypt function after ISC damage, but reports to date leave open the possibility of contributions from "reserve" ISCs (Bankaitis et al., 2018; de Sousa e Melo and de Sauvage, 2019). Substantial crypt recovery after Lgr5⁺ ISC ablation originates in *Bmi1^Cre*-expressing cells (Tian et al., 2011), and although Bmi^hi cells and S-phase LRCs located above the Paneth/ISC zone (Potten, 1998; Sangiorgi and Capecchi, 2008; Yan et al., 2012) contain mainly Paneth and EE cell precursors (Buczacki et al., 2013; Jadhav et al., 2017; Yan et al., 2017), these populations could in principle include putative "reserve" stem cells. Using *Lgr5^Cre*-derived cell labels, we show that nearly all crypt regeneration after lethal damage to Lgr5⁺ ISCs originates in their own recent progeny (i.e., by
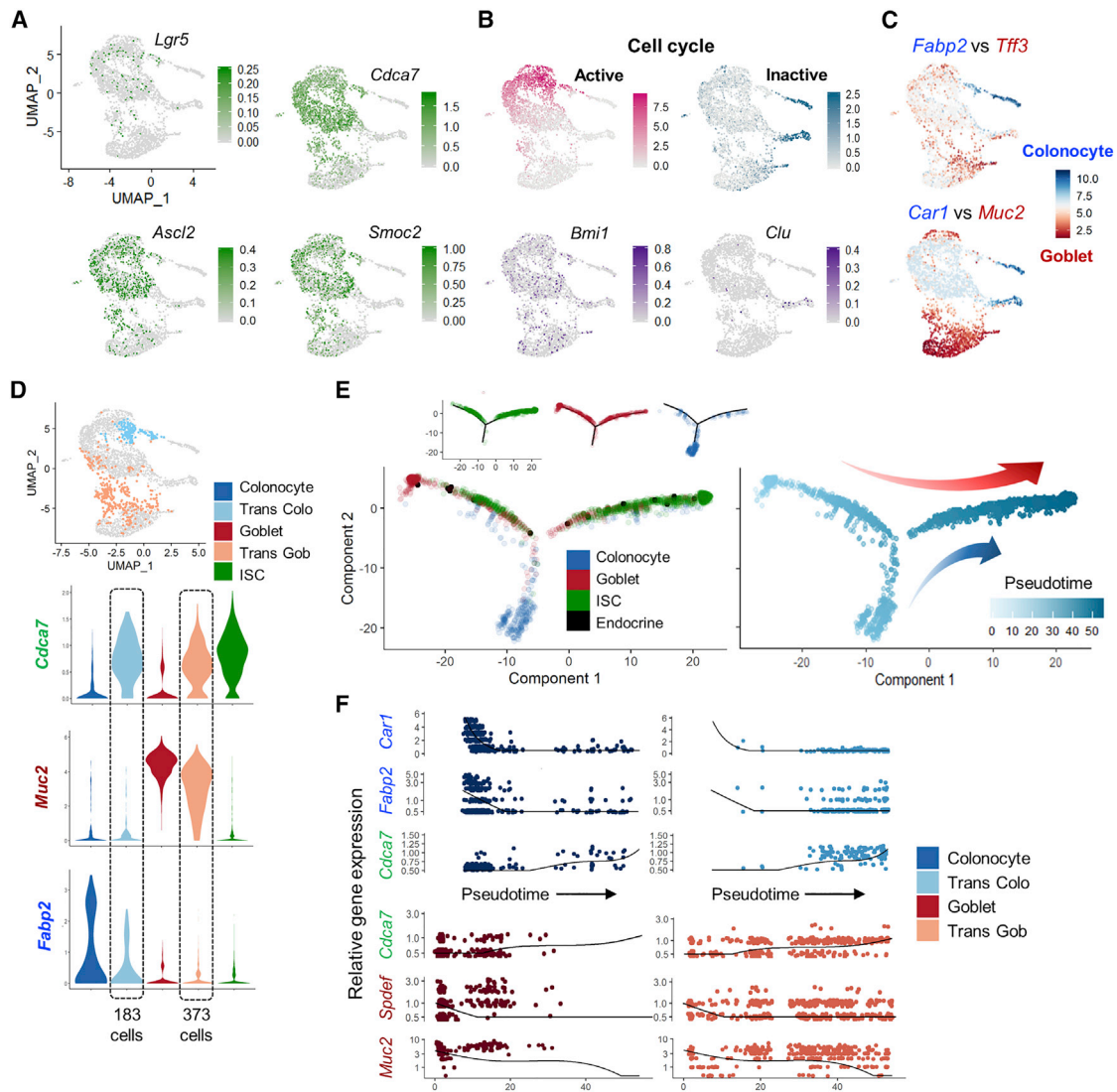
Figure 6. Transcriptomics of ISC Restoration at Single-Cell Resolution

(A) Uniform manifold approximation and projection (UMAP) plots from RNA analysis of 3,254 individual mCh⁺ regenerating "upper" cells, showing the paucity of Lgr5 expression compared with *Ascl2* and other ISC markers, including *Cdca7* and *Smoc2*. In nearest-neighbor depiction, Lgr5⁻ ISC-like cells cluster together. Expression scales are different for each marker.

(B) Within the same UMAP-specified cell groups. Top: distributions of actively cycling and non-replicating cells; bottom: expression of +4 "reserve" ISC marker genes *Bmi1* and *Clu*.

(C) Projection of colonocyte (*Fabp2*, *Car1*) and goblet cell (*Tff3*, *Muc2*) markers on the same UMAP plot reveals that non-cycling mCh⁺ "upper" cells are similar to mature epithelial cells.

(D) Hundreds of cells that cluster at the junctions of mature and ISC-like cells co-express ISC and either colonocyte (e.g., *Fabp2*) or goblet cell (e.g., *Muc2*) markers. In the dedifferentiation context, we therefore consider them bona fide transitional (Trans) cells.

(E) Analysis of scRNA-seq data in Monocle version 2.12.0 (Trapnell et al., 2014). Left: depiction of cells along the defined trajectory, color-coded according to categories defined in UMAP analysis by expression of cell-specific marker genes. Inset: ISCs, goblet cells, and colonocytes projected separately on the trajectory. Right: cells are color-coded according to their imputed pseudotime, with high ISC marker-expressing cells as the destination.

(F) Colonocyte (*Car1*, *Fabp2*), ISC (*Cdca7*), and goblet cell (*Spdef*, *Muc2*) marker expression in mature and transitional (Trans) plotted along the above-defined pseudotime axis. Fall of mature cell, and rise of ISC, markers occurs faster in dedifferentiating colonocytes than in goblet cells. In this interpretation, Trans colonocytes are fewer than Trans goblet cells because the latter dedifferentiate over a longer period.

See also Figure S6.

dedifferentiation), not by recruiting "reserve" ISCs. Moreover, neither "reserve" nor recently reported "revival" ISCs (Ayyaz et al., 2019) exist in numbers sufficient to account for extensive ISC restoration at the observed speed, and our bulk and scRNA profiles of regenerating colonic crypt cells lacked enrichment of +4 cell markers. *Bmi1^Cre*-derived crypt recovery after ISC ablation (Tian et al., 2011) likely reflects *Bmi1* expression in a large fraction of crypt cells (Itzkovitz et al., 2011; Muñoz et al.,
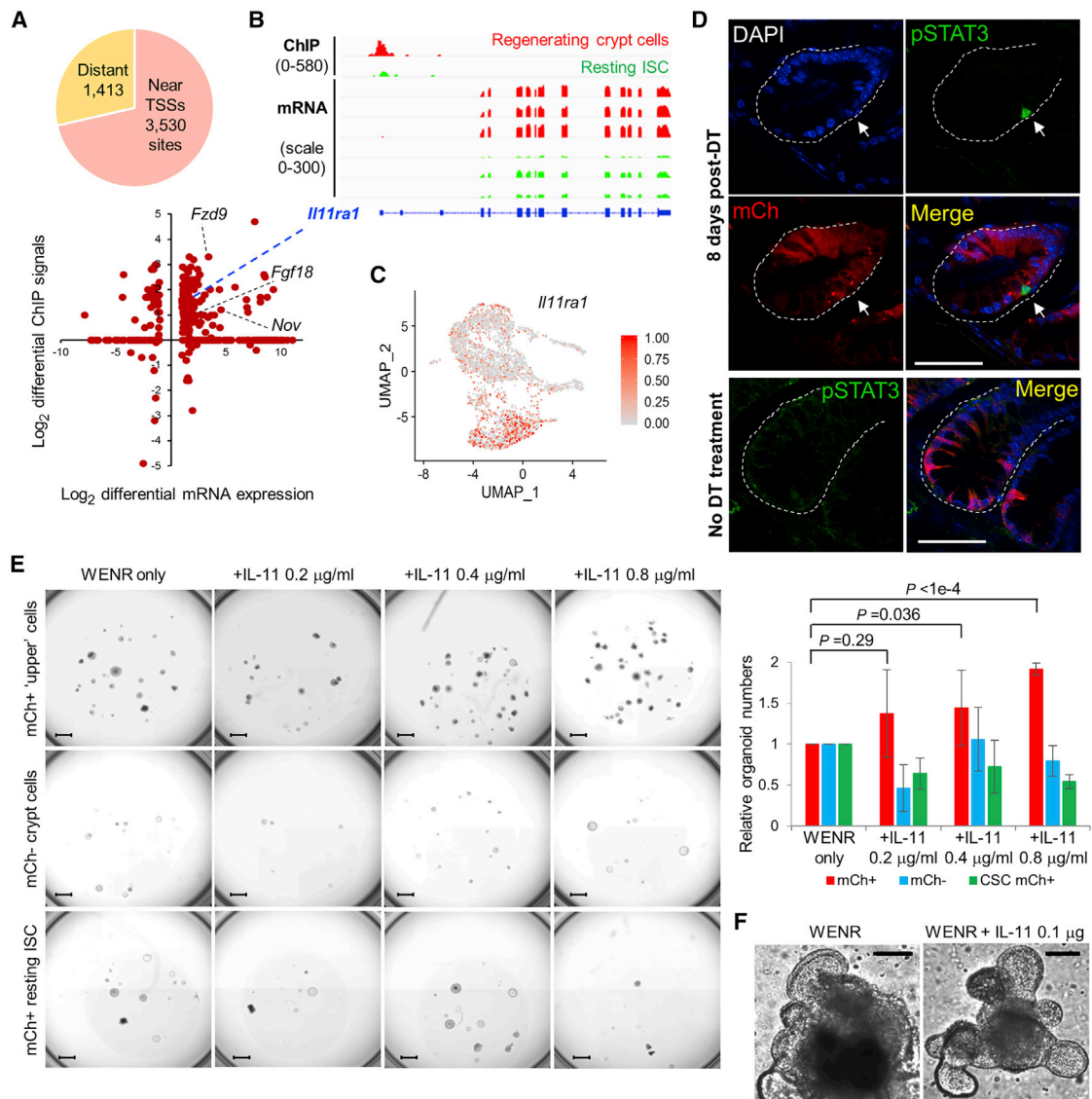
Figure 7. Transcriptional Targets of ASCL2 in ISC Regeneration

(A) Fraction of ASCL2[Flag] chromatin immunoprecipitation sequencing (ChIP-seq) peaks (Table S3) present <1 kb (designated promoters) or >1 kb (presumptive enhancers) from transcription start sites (TSSs) in regenerating Ascl2+ cells. The graph shows the relation between 316 genes differentially expressed in "upper" cells (compared with resting ISCs; Table S1) and relative ASCL2[Flag] ChIP-seq signals at their respective promoters in the two populations. Dashed lines point to candidate ASCL2 target genes that encode signaling factors.

(B) Integrated Genome Viewer (IGV) tracks of RNA-seq and ASCL2[Flag] ChIP-seq data from uninjured colonic ISCs and regenerating day 8 mCh+ crypt cells, showing differential ASCL2 occupancy at the *Il11ra1* promoter and reproducibly increased *Il11ra1* mRNA in the latter cells.

(C) Projection of *Il11ra1* mRNA levels onto the t-distributed stochastic neighbor embedding (tSNE) plot from single regenerating cells (Figure 6), showing its broad distribution and particular enrichment in the goblet cell fraction.

(D) Phosphorylated (p) STAT3 immunofluorescence, showing its presence in rare crypts (≤10 per colon, n = 5 mice) after ISC ablation, compared to absence of pSTAT3 (0 crypts/colon, n = 5 mice) in the absence of ISC injury.

(E) Response of GFP− mCh+ "upper" cells, mCh− crypt cells post-ISC ablation, and uninjured mCh+ resting ISCs to recombinant IL-11 in organoid formation (n = 4 mice). Each image is a composite of multiple overlaid photomicrographs. Scale bars, 1 mm. Bars in the graph represent mean (±SD) ratios of organoids generated with or without rIL-11. Relative organoid numbers in IL-11-treated cultures are expressed in relation to those that each population yielded in WENR medium without IL-11.

(F) Representative structures derived at the first passage of mCh+ "upper" crypt cells initially cultured with rIL-11, indicating that they contained ISCs.

See also Figure S7 and Table S3.

2012), whereas GFP expression in *Bmi1*[Gfp] mice is fortuitously restricted to EE cells enriched in the +4 tier (Buczacki et al., 2013; Jadhav et al., 2017; Yan et al., 2017).

Several observations indicate that diverse crypt progenitors are able to dedifferentiate. First, although we did not strictly compare regenerative efficiencies of Sec and Ent cells, each

lineage readily restores ISCs when the other is absent. Second, after lethal ISC injury, *Ascl2* (mCh) appears in high colonic crypt tiers, which normally lack expression, and *Ascl2*⁺ cells move into the ISC zone, where they later express *Lgr5* (GFP). ASCL2 is required for crypt regeneration, and this ectopic, likely homeostatic, *Ascl2* expression is not confined to rare cells but evident in a large fraction of GFP⁻ crypt cells that we could purify. The short time between administration of DT and appearance of ectopic mCh⁺ cells suggests that *Ascl2* was activated *de novo* in diverse crypt cells, not in clones expanded from rare "reserve" cells. Third, we previously observed extensive changes in mRNA levels and ATAC signals as purified EE and goblet cell precursors were dedifferentiating (Jadhav et al., 2017); such signals would be detected only if they occur in a sizable fraction of cells. Fourth, scRNA-seq analysis of mCh⁺ "upper" cells showed both goblet cell and colonocyte streams converging onto restored ISCs, with seemingly distinct temporal dynamics. Competitive repopulation studies may in the future reveal if restorative contributions from Sec and Ent cells are quantitatively different and occur at different speeds.

ISC-depleted colonic crypts express *Ascl2* (mCh) only eight or nine cell tiers higher than normal. It is therefore unclear if regenerative potential is restricted to progenitors or extends to terminally differentiated cells. In the small intestine, Paneth cell dedifferentiation (Jones et al., 2019; Schmitt et al., 2018; Yu et al., 2018) and ectopic crypt formation along bone morphogenetic protein-inhibited villi (Batts et al., 2006; Haramis et al., 2004) hint that some mature epithelial cells may harbor that capacity. YAP/TAZ signaling and a developmental transcriptional program were recently implicated in ISC regeneration (Gregorieff et al., 2015; Nusse et al., 2018; Yui et al., 2018). Our findings suggest that these conclusions may reflect unique properties of cultured late fetal ISCs rather than epithelial genesis per se. *Ascl2* expression in mCh⁺ "upper" cells is not confined to actively cycling single cells (Figures 6A and 6B), but our experiments do not distinguish whether it is required for crypt cells to dedifferentiate or to expand. Resting ISCs are uniquely sensitive to ~10 Gy γ-irradiation, while other crypt cells survive that dose (Potten, 1998). After ISC ablation, however, regenerating crypt cells become exquisitely radiosensitive (Metcalfe et al., 2014). Consequences of ASCL2 activity, present in resting ISCs and initiated early during progenitor dedifferentiation, may underlie this sensitivity.

Various immune signals are implicated in the regenerative response (Biton et al., 2018; Zhou et al., 2013). IL-11 in particular, possibly from a myofibroblast source (Bamba et al., 2003), aids in intestinal mucosal recovery from bowel resection (Liu et al., 1996), radiation (Potten, 1996), and other ablative injuries (Du et al., 1994). However, it is unclear which crypt cells respond to IL-11 and whether this ability is constitutive or induced upon ISC attrition. We find that resting ISCs express little *Il11ra1*, and levels are elevated in regenerating *Ascl2*⁺ crypt cells. Moreover, unlike native colonic ISCs, regenerating cells respond to rIL-11 with enhanced spheroid formation *in vitro*. ISC-depleted crypts are thus uniquely sensitive to IL-11, which augments dedifferentiation and is probably one of several immune and non-immune signals that help restore ISCs. As a TF essential to the process, ASCL2 helps orchestrate that robust homeostatic response.

STAR★METHODS

Detailed methods are provided in the online version of this paper and include the following:

- KEY RESOURCES TABLE
- LEAD CONTACT AND MATERIALS AVAILABILITY
- EXPERIMENTAL MODEL AND SUBJECT DETAILS
  ○ Animals
- METHOD DETAILS
  ○ Mouse treatments
  ○ Detection of fluorescent cells in tissues
  ○ Immunofluorescence
  ○ Colonic cell isolation
  ○ Culture and analysis of colonic organoids
  ○ RNA isolation and sequencing
  ○ Chromatin immunoprecipitation (ChIP-seq)
- QUANTIFICATION AND STATISTICAL ANALYSIS
  ○ General
  ○ Computational analyses
  ○ Single-cell RNA-seq
  ○ Mathematical modeling to quantify relative fitness of Ascl2⁻/⁻ ISCs
- DATA AND CODE AVAILABILITY

REFERENCES

Anders, S., Pyl, P.T., and Huber, W. (2015). HTSeq—a Python framework to work with high-throughput sequencing data. Bioinformatics *31*, 166–169.

Ayyaz, A., Kumar, S., Sangiorgi, B., Ghoshal, B., Gosio, J., Ouladan, S., Fink, M., Barutcu, S., Trcka, D., Shen, J., et al. (2019). Single-cell transcriptomes of the regenerating intestine reveal a revival stem cell. Nature *569*, 121–125.

Bamba, S., Andoh, A., Yasui, H., Makino, J., Kim, S., and Fujiyama, Y. (2003). Regulation of IL-11 expression in intestinal myofibroblasts: role of c-Jun AP-1- and MAPK-dependent pathways. Am. J. Physiol. Gastrointest. Liver Physiol. *285*, G529–G538.

Banerjee, K.K., Saxena, M., Kumar, N., Chen, L., Cavazza, A., Toke, N.H., O'Neill, N.K., Madha, S., Jadhav, U., Verzi, M.P., and Shivdasani, R.A. (2018). Enhancer, transcriptional, and cell fate plasticity precedes intestinal determination during endoderm development. Genes Dev. *32*, 1430–1442.

Bankaitis, E.D., Ha, A., Kuo, C.J., and Magness, S.T. (2018). Reserve stem cells in intestinal homeostasis and injury. Gastroenterology *155*, 1348–1361.

Barker, N., van Es, J.H., Kuipers, J., Kujala, P., van den Born, M., Cozijnsen, M., Haegebarth, A., Korving, J., Begthel, H., Peters, P.J., and Clevers, H. (2007). Identification of stem cells in small intestine and colon by marker gene Lgr5. Nature *449*, 1003–1007.

Barker, N., van Oudenaarden, A., and Clevers, H. (2012). Identifying the stem cell of the intestinal crypt: strategies and pitfalls. Cell Stem Cell *11*, 452–460.

Batts, L.E., Polk, D.B., Dubois, R.N., and Kulessa, H. (2006). Bmp signaling is required for intestinal growth and morphogenesis. Dev. Dyn. *235*, 1563–1570.

Biton, M., Haber, A.L., Rogel, N., Burgin, G., Beyaz, S., Schnell, A., Ashenberg, O., Su, C.W., Smillie, C., Shekhar, K., et al. (2018). T helper cell cytokines modulate intestinal stem cell renewal and differentiation. Cell *175*, 1307–1320.e22.

Buczacki, S.J., Zecchini, H.I., Nicholson, A.M., Russell, R., Vermeulen, L., Kemp, R., and Winton, D.J. (2013). Intestinal label-retaining cells are secretory precursors expressing Lgr5. Nature *495*, 65–69.

Butler, A., Hoffman, P., Smibert, P., Papalexi, E., and Satija, R. (2018). Integrating single-cell transcriptomic data across different conditions, technologies, and species. Nat. Biotechnol. *36*, 411–420.

Castillo-Azofeifa, D., Fazio, E.N., Nattiv, R., Good, H.J., Wald, T., Pest, M.A., de Sauvage, F.J., Klein, O.D., and Asfaha, S. (2019). Atoh1+ secretory progenitors possess renewal capacity independent of Lgr5+ cells during colonic regeneration. EMBO J. *38*, e99984.

Chaves-Perez, A., Yilmaz, M., Perna, C., de la Rosa, S., and Djouder, N. (2019). URI is required to maintain intestinal architecture during ionizing radiation. Science *364*, eaaq1165.

Cheng, H., and Bjerknes, M. (1985). Whole population cell kinetics and post-natal development of the mouse intestinal epithelium. Anat. Rec. *211*, 420–426.

Corces, M.R., Trevino, A.E., Hamilton, E.G., Greenside, P.G., Sinnott-Armstrong, N.A., Vesuna, S., Satpathy, A.T., Rubin, A.J., Montine, K.S., Wu, B., et al. (2017). An improved ATAC-seq protocol reduces background and enables interrogation of frozen tissues. Nat. Methods *14*, 959–962.

Cornwell, M., Vangala, M., Taing, L., Herbert, Z., Köster, J., Li, B., Sun, H., Li, T., Zhang, J., Qiu, X., et al. (2018). VIPER: Visualization Pipeline for RNA-seq, a Snakemake workflow for efficient and complete RNA-seq analysis. BMC Bioinformatics *19*, 135.

de Sousa e Melo, F., and de Sauvage, F.J. (2019). Cellular plasticity in intestinal homeostasis and disease. Cell Stem Cell *24*, 54–64.

Dobin, A., Davis, C.A., Schlesinger, F., Drenkow, J., Zaleski, C., Jha, S., Batut, P., Chaisson, M., and Gingeras, T.R. (2013). STAR: ultrafast universal RNA-seq aligner. Bioinformatics *29*, 15–21.

Du, X.X., Doerschuk, C.M., Orazi, A., and Williams, D.A. (1994). A bone marrow stromal-derived growth factor, interleukin-11, stimulates recovery of small intestinal mucosal cells after cytoablative therapy. Blood *83*, 33–37.

el Marjou, F., Janssen, K.P., Chang, B.H., Li, M., Hindie, V., Chan, L., Louvard, D., Chambon, P., Metzger, D., and Robine, S. (2004). Tissue-specific and inducible Cre-mediated recombination in the gut epithelium. Genesis *39*, 186–193.

Fordham, R.P., Yui, S., Hannan, N.R., Soendergaard, C., Madgwick, A., Schweiger, P.J., Nielsen, O.H., Vallier, L., Pedersen, R.A., Nakamura, T., et al. (2013). Transplantation of expanded fetal intestinal progenitors contributes to colon regeneration after injury. Cell Stem Cell *13*, 734–744.

Gregorieff, A., Liu, Y., Inanlou, M.R., Khomchuk, Y., and Wrana, J.L. (2015). Yap-dependent reprogramming of Lgr5(+) stem cells drives intestinal regeneration and cancer. Nature *526*, 715–718.

Han, H., Tanigaki, K., Yamamoto, N., Kuroda, K., Yoshimoto, M., Nakahata, T., Ikuta, K., and Honjo, T. (2002). Inducible gene knockout of transcription factor recombination signal binding protein-J reveals its essential role in T versus B lineage decision. Int. Immunol. *14*, 637–645.

Haramis, A.P., Begthel, H., van den Born, M., van Es, J., Jonkheer, S., Offerhaus, G.J., and Clevers, H. (2004). De novo crypt formation and juvenile polyposis on BMP inhibition in mouse intestine. Science *303*, 1684–1686.

Hulsen, T., de Vlieg, J., and Alkema, W. (2008). BioVenn - a web application for the comparison and visualization of biological lists using area-proportional Venn diagrams. BMC Genomics *9*, 488.

Ishibashi, F., Shimizu, H., Nakata, T., Fujii, S., Suzuki, K., Kawamoto, A., Anzai, S., Kuno, R., Nagata, S., Ito, G., et al. (2018). Contribution of ATOH1+ cells to the homeostasis, repair, and tumorigenesis of the colonic epithelium. Stem Cell Reports *10*, 27–42.

Itzkovitz, S., Lyubimova, A., Blat, I.C., Maynard, M., van Es, J., Lees, J., Jacks, T., Clevers, H., and van Oudenaarden, A. (2011). Single-molecule transcript counting of stem-cell markers in the mouse intestine. Nat. Cell Biol. *14*, 106–114.

Jadhav, U., Saxena, M., O'Neill, N.K., Saadatpour, A., Yuan, G.C., Herbert, Z., Murata, K., and Shivdasani, R.A. (2017). Dynamic reorganization of chromatin accessibility signatures during dedifferentiation of secretory precursors into Lgr5+ intestinal stem cells. Cell Stem Cell *21*, 65–77.e5.

Jenkins, B.J., Roberts, A.W., Greenhill, C.J., Najdovska, M., Lundgren-May, T., Robb, L., Grail, D., and Ernst, M. (2007). Pathologic consequences of STAT3 hyperactivation by IL-6 and IL-11 during hematopoiesis and lymphopoiesis. Blood *109*, 2380–2388.

Jones, J.C., Brindley, C.D., Elder, N.H., Myers, M.G., Jr., Rajala, M.W., Dekaney, C.M., McNamee, E.N., Frey, M.R., Shroyer, N.F., and Dempsey, P.J. (2019). Cellular plasticity of Defa4(Cre)-expressing Paneth cells in response to Notch activation and intestinal injury. Cell. Mol. Gastroenterol. Hepatol. *7*, 533–554.

Jubb, A.M., Chalasani, S., Frantz, G.D., Smits, R., Grabsch, H.I., Kavi, V., Maughan, N.J., Hillan, K.J., Quirke, P., and Koeppen, H. (2006). Achaete-scute like 2 (ascl2) is a target of Wnt signalling and is upregulated in intestinal neoplasia. Oncogene *25*, 3445–3457.

Kim, T.H., Li, F., Ferreiro-Neira, I., Ho, L.L., Luyten, A., Nalapareddy, K., Long, H., Verzi, M., and Shivdasani, R.A. (2014). Broadly permissive intestinal chromatin underlies lateral inhibition and cell plasticity. Nature *506*, 511–515.

Kozar, S., Morrissey, E., Nicholson, A.M., van der Heijden, M., Zecchini, H.I., Kemp, R., Tavaré, S., Vermeulen, L., and Winton, D.J. (2013). Continuous clonal labeling reveals small numbers of functional stem cells in intestinal crypts and adenomas. Cell Stem Cell *13*, 626–633.

Langmead, B., and Salzberg, S.L. (2012). Fast gapped-read alignment with Bowtie 2. Nat. Methods *9*, 357–359.

Li, L., and Clevers, H. (2010). Coexistence of quiescent and active adult stem cells in mammals. Science *327*, 542–545.

Liu, Q., Du, X.X., Schindel, D.T., Yang, Z.X., Rescorla, F.J., Williams, D.A., and Grosfeld, J.L. (1996). Trophic effects of interleukin-11 in rats with experimental short bowel syndrome. J. Pediatr. Surg. *31*, 1047–1050, discussion 1050–1051.

Lopez-Garcia, C., Klein, A.M., Simons, B.D., and Winton, D.J. (2010). Intestinal stem cell replacement follows a pattern of neutral drift. Science *330*, 822–825.

Love, M.I., Huber, W., and Anders, S. (2014). Moderated estimation of fold change and dispersion for RNA-seq data with DESeq2. Genome Biol. *15*, 550.

Madisen, L., Zwingman, T.A., Sunkin, S.M., Oh, S.W., Zariwala, H.A., Gu, H., Ng, L.L., Palmiter, R.D., Hawrylycz, M.J., Jones, A.R., et al. (2010). A robust and high-throughput Cre reporting and characterization system for the whole mouse brain. Nat. Neurosci. *13*, 133–140.

Mao, Q., Wang, L., Goodison, S., and Sun, Y. (2015). Dimensionality reduction via graph structure learning. In KKD '15: Proceedings of the 21st ACM SIGKDD International Conference on Knowledge Discovery and Data Mining, pp. 765–774.

Metcalfe, C., Kljavin, N.M., Ybarra, R., and de Sauvage, F.J. (2014). Lgr5+ stem cells are indispensable for radiation-induced intestinal regeneration. Cell Stem Cell *14*, 149–159.

Montgomery, R.K., Carlone, D.L., Richmond, C.A., Farilla, L., Kranendonk, M.E., Henderson, D.E., Baffour-Awuah, N.Y., Ambruzs, D.M., Fogli, L.K., Algra, S., and Breault, D.T. (2011). Mouse telomerase reverse transcriptase (mTert) expression marks slowly cycling intestinal stem cells. Proc. Natl. Acad. Sci. U S A *108*, 179–184.

Muñoz, J., Stange, D.E., Schepers, A.G., van de Wetering, M., Koo, B.K., Itzkovitz, S., Volckmann, R., Kung, K.S., Koster, J., Radulescu, S., et al. (2012). The Lgr5 intestinal stem cell signature: robust expression of proposed quiescent '+4' cell markers. EMBO J. *31*, 3079–3091.

Mustata, R.C., Vasile, G., Fernandez-Vallone, V., Strollo, S., Lefort, A., Libert, F., Monteyne, D., Pérez-Morga, D., Vassart, G., and Garcia, M.I. (2013). Identification of Lgr5-independent spheroid-generating progenitors of the mouse fetal intestinal epithelium. Cell Rep. *5*, 421–432.

Nusse, Y.M., Savage, A.K., Marangoni, P., Rosendahl-Huber, A.K.M., Landman, T.A., de Sauvage, F.J., Locksley, R.M., and Klein, O.D. (2018). Parasitic helminths induce fetal-like reversion in the intestinal stem cell niche. Nature *559*, 109–113.

Ootani, A., Li, X., Sangiorgi, E., Ho, Q.T., Ueno, H., Toda, S., Sugihara, H., Fujimoto, K., Weissman, I.L., Capecchi, M.R., and Kuo, C.J. (2009). Sustained in vitro intestinal epithelial culture within a Wnt-dependent stem cell niche. Nat. Med. *15*, 701–706.

Pinello, L., Xu, J., Orkin, S.H., and Yuan, G.C. (2014). Analysis of chromatin-state plasticity identifies cell-type-specific regulators of H3K27me3 patterns. Proc. Natl. Acad. Sci. U S A *111*, E344–E353.

Potten, C.S. (1996). Protection of the small intestinal clonogenic stem cells from radiation-induced damage by pretreatment with interleukin 11 also increases murine survival time. Stem Cells *14*, 452–459.

Potten, C.S. (1998). Stem cells in gastrointestinal epithelium: numbers, characteristics and death. Philos. Trans. R. Soc. Lond. B Biol. Sci. *353*, 821–830.

Quinlan, A.R., and Hall, I.M. (2010). BEDTools: a flexible suite of utilities for comparing genomic features. Bioinformatics *26*, 841–842.

R Core Team (2013). R: A language and environment for statistical computing (Vienna, Austria: R Foundation for Statistical Computing).

Ramírez, F., Ryan, D.P., Grüning, B., Bhardwaj, V., Kilpert, F., Richter, A.S., Heyne, S., Dündar, F., and Manke, T. (2016). deepTools2: a next generation web server for deep-sequencing data analysis. Nucleic Acids Res. *44* (W1), W160–W165.

Robinson, J.T., Thorvaldsdóttir, H., Winckler, W., Guttman, M., Lander, E.S., Getz, G., and Mesirov, J.P. (2011). Integrative genomics viewer. Nat. Biotechnol. *29*, 24–26.

San Roman, A.K., Tovaglieri, A., Breault, D.T., and Shivdasani, R.A. (2015). Distinct processes and transcriptional targets underlie CDX2 requirements in intestinal stem cells and differentiated villus cells. Stem Cell Reports *5*, 673–681.

Sangiorgi, E., and Capecchi, M.R. (2008). Bmi1 is expressed in vivo in intestinal stem cells. Nat. Genet. *40*, 915–920.

Santos, A.J.M., Lo, Y.H., Mah, A.T., and Kuo, C.J. (2018). The intestinal stem cell niche: Homeostasis and adaptations. Trends Cell Biol. *28*, 1062–1078.

Sasaki, N., Sachs, N., Wiebrands, K., Ellenbroek, S.I., Fumagalli, A., Lyubimova, A., Begthel, H., van den Born, M., van Es, J.H., Karthaus, W.R., et al. (2016). Reg4+ deep crypt secretory cells function as epithelial niche for Lgr5+ stem cells in colon. Proc. Natl. Acad. Sci. U S A *113*, E5399–E5407.

Sato, T., Vries, R.G., Snippert, H.J., van de Wetering, M., Barker, N., Stange, D.E., van Es, J.H., Abo, A., Kujala, P., Peters, P.J., and Clevers, H. (2009). Single Lgr5 stem cells build crypt-villus structures in vitro without a mesenchymal niche. Nature *459*, 262–265.

Schindelin, J., Arganda-Carreras, I., Frise, E., Kaynig, V., Longair, M., Pietzsch, T., Preibisch, S., Rueden, C., Saalfeld, S., Schmid, B., et al. (2012). Fiji: an open-source platform for biological-image analysis. Nat. Methods *9*, 676–682.

Schmitt, M., Schewe, M., Sacchetti, A., Feijtel, D., van de Geer, W.S., Teeuwssen, M., Sleddens, H.F., Joosten, R., van Royen, M.E., van de Werken, H.J.G., et al. (2018). Paneth cells respond to inflammation and contribute to tissue regeneration by acquiring stem-like features through SCF/c-Kit signaling. Cell Rep. *24*, 2312–2328.e17.

Schuijers, J., Junker, J.P., Mokry, M., Hatzis, P., Koo, B.K., Sasselli, V., van der Flier, L.G., Cuppen, E., van Oudenaarden, A., and Clevers, H. (2015). Ascl2 acts as an R-spondin/Wnt-responsive switch to control stemness in intestinal crypts. Cell Stem Cell *16*, 158–170.

Shen, L., Shao, N.Y., Liu, X., Maze, I., Feng, J., and Nestler, E.J. (2013). diffReps: detecting differential chromatin modification sites from ChIP-seq data with biological replicates. PLoS ONE *8*, e65598.

Shroyer, N.F., Helmrath, M.A., Wang, V.Y., Antalffy, B., Henning, S.J., and Zoghbi, H.Y. (2007). Intestine-specific ablation of mouse atonal homolog 1 (Math1) reveals a role in cellular homeostasis. Gastroenterology *132*, 2478–2488.

Snippert, H.J., van der Flier, L.G., Sato, T., van Es, J.H., van den Born, M., Kroon-Veenboer, C., Barker, N., Klein, A.M., van Rheenen, J., Simons, B.D., and Clevers, H. (2010). Intestinal crypt homeostasis results from neutral competition between symmetrically dividing Lgr5 stem cells. Cell *143*, 134–144.

Snippert, H.J., Schepers, A.G., van Es, J.H., Simons, B.D., and Clevers, H. (2014). Biased competition between Lgr5 intestinal stem cells driven by oncogenic mutation induces clonal expansion. EMBO Rep. *15*, 62–69.

Subramanian, A., Tamayo, P., Mootha, V.K., Mukherjee, S., Ebert, B.L., Gillette, M.A., Paulovich, A., Pomeroy, S.L., Golub, T.R., Lander, E.S., et al. (2005). Gene set enrichment analysis: a knowledge-based approach for interpreting genome-wide expression profiles. Proc. Natl. Acad Sci. USA *102*, 15545–15550.

Takeda, N., Jain, R., LeBoeuf, M.R., Wang, Q., Lu, M.M., and Epstein, J.A. (2011). Interconversion between intestinal stem cell populations in distinct niches. Science *334*, 1420–1424.

Tetteh, P.W., Basak, O., Farin, H.F., Wiebrands, K., Kretzschmar, K., Begthel, H., van den Born, M., Korving, J., de Sauvage, F., van Es, J.H., et al. (2016). Replacement of lost Lgr5-positive stem cells through plasticity of their enterocyte-lineage daughters. Cell Stem Cell *18*, 203–213.

Tian, H., Biehs, B., Warming, S., Leong, K.G., Rangell, L., Klein, O.D., and de Sauvage, F.J. (2011). A reserve stem cell population in small intestine renders Lgr5-positive cells dispensable. Nature *478*, 255–259.

Tomic, G., Morrissey, E., Kozar, S., Ben-Moshe, S., Hoyle, A., Azzarelli, R., Kemp, R., Chilamakuri, C.S.R., Itzkovitz, S., Philpott, A., et al. (2018). Phospho-regulation of ATOH1 is required for plasticity of secretory progenitors and tissue regeneration. Cell Stem Cell *23*, 436–443.e7.

Trapnell, C., Cacchiarelli, D., Grimsby, J., Pokharel, P., Li, S., Morse, M., Lennon, N.J., Livak, K.J., Mikkelsen, T.S., and Rinn, J.L. (2014). The dynamics and regulators of cell fate decisions are revealed by pseudotemporal ordering of single cells. Nat. Biotechnol. *32*, 381–386.

van der Flier, L.G., van Gijn, M.E., Hatzis, P., Kujala, P., Haegebarth, A., Stange, D.E., Begthel, H., van den Born, M., Guryev, V., Oving, I., et al. (2009). Transcription factor achaete scute-like 2 controls intestinal stem cell fate. Cell *136*, 903–912.

van Es, J.H., Sato, T., van de Wetering, M., Lyubimova, A., Yee Nee, A.N., Gregorieff, A., Sasaki, N., Zeinstra, L., van den Born, M., Korving, J., et al. (2012). Dll1+ secretory progenitor cells revert to stem cells upon crypt damage. Nat. Cell Biol. *14*, 1099–1104.

Vermeulen, L., Morrissey, E., van der Heijden, M., Nicholson, A.M., Sottoriva, A., Buczacki, S., Kemp, R., Tavaré, S., and Winton, D.J. (2013). Defining stem cell dynamics in models of intestinal tumor initiation. Science *342*, 995–998.

Wickham, H. (2009). ggplot2: Elegant graphics for data analysis (New York: Springer-Verlag).

Yan, K.S., Chia, L.A., Li, X., Ootani, A., Su, J., Lee, J.Y., Su, N., Luo, Y., Heilshorn, S.C., Amieva, M.R., et al. (2012). The intestinal stem cell markers Bmi1 and Lgr5 identify two functionally distinct populations. Proc. Natl. Acad. Sci. U S A *109*, 466–471.

Yan, K.S., Gevaert, O., Zheng, G.X.Y., Anchang, B., Probert, C.S., Larkin, K.A., Davies, P.S., Cheng, Z.F., Kaddis, J.S., Han, A., et al. (2017). Intestinal enteroendocrine lineage cells possess homeostatic and injury-inducible stem cell activity. Cell Stem Cell *21*, 78–90.e6.

Yousefi, M., Li, L., and Lengner, C.J. (2017). Hierarchy and plasticity in the intestinal stem cell compartment. Trends Cell Biol. *27*, 753–764.

Yu, S., Tong, K., Zhao, Y., Balasubramanian, I., Yap, G.S., Ferraris, R.P., Bonder, E.M., Verzi, M.P., and Gao, N. (2018). Paneth cell multipotency induced by Notch activation following injury. Cell Stem Cell *23*, 46–59.e5.

Yui, S., Azzolin, L., Maimets, M., Pedersen, M.T., Fordham, R.P., Hansen, S.L., Larsen, H.L., Guiu, J., Alves, M.R.P., Rundsten, C.F., et al. (2018). YAP/TAZ-dependent reprogramming of colonic epithelium links ECM remodeling to tissue regeneration. Cell Stem Cell *22*, 35–49.e7.

Zhang, Y., Liu, T., Meyer, C.A., Eeckhoute, J., Johnson, D.S., Bernstein, B.E., Nusbaum, C., Myers, R.M., Brown, M., Li, W., and Liu, X.S. (2008). Model-based analysis of ChIP-Seq (MACS). Genome Biol. *9*, R137.

Zhou, W.J., Geng, Z.H., Spence, J.R., and Geng, J.G. (2013). Induction of intestinal stem cells by R-spondin 1 and Slit2 augments chemoradioprotection. Nature *501*, 107–111.

STAR★METHODS

KEY RESOURCES TABLE

REAGENT or RESOURCE	SOURCE	IDENTIFIER
Antibodies		
ANTI-FLAG® M2 antibody	Sigma-Aldrich	Cat# F1804; RRID: AB_262044
Anti-Mouse IL11RA1 antibody	R&D Systems	Cat# AF490; RRID: AB_355391
Anti-Ki-67 antibody	Abcam	Cat# ab15580; RRID: AB_443209
Anti-CLU antibody	R&D Systems	Cat# AF2747; RRID: AB_2083314
Anti-phosphoSTAT3 antibody	Cell Signaling	Cat# 9145; RRID: AB_2491009
Cleaved Caspase3 antibody	Cell Signaling	Cat# 9664; RRID: AB_2070042
Donkey anti-Mouse IgG (H+L) Cross-Adsorbed Secondary Antibody, Alexa Fluor 488	Invitrogen	Cat# A-21202; RRID: AB_141607
Goat anti-Rabbit IgG (H+L) Cross-Adsorbed Secondary Antibody, Alexa Fluor 488	Invitrogen	Cat# A-11034; RRID: AB_2576217
Goat anti-Rabbit IgG (H+L) Cross-Adsorbed Secondary Antibody, Alexa Fluor 594	Invitrogen	Cat# A-11037; RRID: AB_2534095
Biotinylated Goat Anti-Rabbit IgG Antibody	Vector Laboratories	Cat# BA-1000; RRID: AB_2313606
Chemicals, Peptides, and Recombinant Proteins		
Tamoxifen	Sigma-Aldrich	SKU# T5648
Accumax	Innovative Cell Technologies	AM105
Dispase	Stem Cell Technologies	07913
TrypLE Select Enzyme (10X)	Thermo Fisher	A1217702
Advanced DMEM/F-12	Life Technologies	12634010
DMEM	Corning	17-205-CV
HEPES	Life Technologies	15630080
GlutaMAX	Life Technologies	35050061
Penicillin-streptomycin	Life Technologies	15140122
Matrigel, growth factor reduced, phenol red-free	BD Biosciences	356231
N-2 Supplement	Life Technologies	17502001
B-27 Supplement	Life Technologies	17504001
EGF Recombinant Mouse Protein	Life Technologies	PMG8043
Murine Noggin	Peprotech	250-38
Jagged-1	AnaSpec	61298
N-Acetyl-L-cysteine	Sigma-Aldrich	A9165
Recombinant Murine IL-11	Peprotech	220-11
Recombinant Human FGF-18 Protein	R&D Systems	8988-F18-050
Recombinant Mouse NOV/CCN3 Protein	R&D Systems	1976-NV-050
Diphtheria Toxin from *Corynebacterium diphtheriae*	Sigma-Aldrich	D0564-1MG
Critical Commercial Assays		
SMARTer® Universal Low Input RNA Kit	Takara Bio	634940
Nextera DNA Sample Preparation Kit	Illumina	FC-121-1030
Agencourt AMPure XP	Beckman Coulter	A63881
Dynabeads Protein G for Immunoprecipitation	Thermo Fisher	*10004D*
Qubit dsDNA HS Assay Kit	Thermo Fisher	Q32854
QIAquick PCR Purification Kit	QIAGEN	28106
Trizol reagent	Thermo Fisher	15596026
MinElute PCR Purification Kit	QIAGEN	28004
RNeasy Mini Kit	QIAGEN	74104
[REMOVED HYPERLINK FIELD]TURBO DNA-free Kit	Life Technologies	AM1907

(Continued on next page)

Continued

REAGENT or RESOURCE	SOURCE	IDENTIFIER
Agilent High Sensitivity DNA Kit	Agilent Technologies	5067-4626
NEBNext® High-Fidelity 2X PCR Master Mix	NEB	M0541
Vectastain Elite ABC Kit	Vector Laboratories	PK-6100
3,3′ diaminobenzidine tetrahydrochloride	Sigma-Aldrich	D3939
VECTASHIELD Mounting Medium with DAPI	Vector Laboratories	H-1200
Complete, mini protease inhibitor cocktail	Sigma	11836153001
OCT compound	Tissue-Tek	4583
LIVE/DEAD Fixable Far Red Dead Cell Stain Kit	Life Technologies	L10120
SYTOX Blue Dead Cell Stain	Life Technologies	S34857
Chromium Single Cell B Chip	10X Genomics	1000073
Chromium Next GEM Single Cell 3′ GEM, Library & Gel Bead Kit	10X Genomics	1000128
Deposited Data		
Raw and analyzed data	This paper	GEO: GSE130822
Experimental Models: Cell Lines		
L Wnt-3A	ATCC	Cat# CRL-2647; RRID: CVCL_0635
HA-R-Spondin1-Fc293T	Ootani et al., 2009	N/A (gift from Dr. Calvin Kuo, Stanford Univ.)
Experimental Models: Organisms/Strains		
Mouse: $Lgr5^{GFP-Cre-ER(T2)}$	The Jackson Laboratory	MGI:3833921
Mouse: $Lgr5^{Dtr-GFP}$	Tian et al., 2011	MGI:5294798
Mouse: $Villin-Cre^{ER(T2)}$	(el Marjou et al., 2004)	MGI:3053826
Mouse: $Rbpj^{Fl}$	Han et al., 2002	MGI:3583755
Mouse: $Atoh1^{Fl}$	Shroyer et al., 2007	MGI:3767172
Mouse: $R26R^{tdTomato}$	Madisen et al., 2010	MGI:3813512
Mouse: $Ascl2^{Umc}$	van der Flier et al., 2009	MGI:3846671
Mouse: $Ascl2^{Dfci}$	This paper	N/A
Mouse: $FLPo-10$	The Jackson Laboratory	MGI:4455294
Software and Algorithms		
Bedtools	(Quinlan and Hall, 2010)	https://bedtools.readthedocs.io/en/latest/
Bowtie2	(Langmead and Salzberg, 2012)	http://bowtie-bio.sourceforge.net/bowtie2/index.shtml
BioVenn	(Hulsen et al., 2008)	www.biovenn.nl/
deepTools v2.5	(Ramírez et al., 2016)	https://github.com/deeptools/deepTools
DeSeq2	(Love et al., 2014)	http://bioconductor.org/packages/release/bioc/html/DESeq2.html
diffReps	(Shen et al., 2013)	https://github.com/shenlab-sinai/diffreps
Fiji	(Schindelin et al., 2012)	https://fiji.sc/
FlowJo	BD	https://www.flowjo.com/
Gene Set Enrichment Analysis (GSEA)	(Subramanian et al., 2005)	http://software.broadinstitute.org/gsea/index.jsp
ggplot2	(Wickham, 2009)	https://ggplot2.tidyverse.org/
GraphPad Prism 7	N/A	https://www.graphpad.com/scientific-software/prism/
HTSeq v0.6.1	(Anders et al., 2015)	https://www-huber.embl.de/HTSeq/doc/overview.html
IGV	(Robinson et al., 2011)	http://software.broadinstitute.org/software/igv/
MACS2 v1.4	(Zhang et al., 2008)	https://github.com/taoliu/MACS
UCSC Gene ID Converter	Andy Saurin	https://www.biotools.fr/mouse/ucsc_id_converter
R	(R Core Team, 2013)	https://www.R-project.org/
STAR aligner v2.5.3a	(Dobin et al., 2013)	https://github.com/alexdobin/STAR

LEAD CONTACT AND MATERIALS AVAILABILITY

Further information and requests for reagents should be directed to and will be fulfilled by the Lead Contact, Ramesh Shivdasani (ramesh_shivdasani@dfci.harvard.edu), upon execution of a suitable Materials Transfer Agreement. *Ascl2^{Dfci}* mice will be provided directly; in the event of high demand, and presuming the strain will be accepted, the Lead Contact will deposit the strain in the Jackson Laboratories collection.

EXPERIMENTAL MODEL AND SUBJECT DETAILS

Animals

All mouse strains (*Lgr5$^{GFP-Cre}$*, *Lgr5$^{Dtr-GFP}$*, *R26R^{tdTomato}*, *Villin-Cre^{ER-T2}*, *Atoh1^{Fl}*, *Rbpj^{Fl}*, *Ascl2^{Dfci}*, *Ascl2^{Umc}*, and *Apc^{Fl}*) were maintained on a predominantly C57BL/6 background. Mouse sources and citations are provided in the Key Resources Table. Animals were housed under specific pathogen-free conditions in 12-hour light/dark cycles at 23 ± 1°C and humidity 55 ± 15%. Food and water were provided *ad libitum*. Animals were weaned 21 to 28 days after birth and handled and euthanized according to procedures approved by the Animal Care and Use Committee of the Dana-Farber Cancer Institute. Mice were at least 8 weeks old at the time of experiments and cell isolations. Mice of the both sexes were used in most experiments, with littermate controls.

To generate *Ascl2^{Dfci}* mice, the two *Ascl2* homology arms and 3XFLAG-tagged *Ascl2* cDNA were cloned by high-fidelity PCR from C57BL/6 genomic DNA. mCherry cDNA was extracted from the plasmid pEF1alpha-mCherry (Takara, 631969) and all fragments were moved into the targeting vector (Figure S1D). The targeting construct was verified by DNA sequencing, linearized, and electroporated into JM8.N4 male embryonic stem cells (ESC), which were selected in medium containing G418 and gancyclovir. Recombinant ESC clones were identified by long-range PCR across the *Ascl2* locus and injected into C57BL/6-albino blastocysts. Founder males, identified by PCR analysis of tail DNA, were bred to *B6.Cg-Tg(Pgk1-Flpo)10^{Sykr}/J* females (*FLPo-10*, Jackson Laboratories stock #011065) to delete the *Neo^R* cassette. As we expanded the *Ascl2^{Dfci}* colony by crossing with *Lgr5$^{GFP-Cre}$*, *Lgr5$^{Dtr-GFP}$*, or *Villin-Cre^{ER-T2}* mice, mice carrying *FLPo-10* were excluded and we verified the whole *Ascl2^{Dfci}* locus by sequencing genomic DNA. Except where stated otherwise (e.g., Figure 4), *Ascl2$^{Fl/Fl}$* and *Ascl2$^{-/-}$* refer to any combination of the *Ascl2^{Dfci}* and *Ascl2^{Umc}* alleles.

METHOD DETAILS

Mouse treatments

To delete floxed *Atoh1* alleles, we administered 1 mg tamoxifen (Sigma-Aldrich, T5648; stock solutions prepared in cornflower oil) by intraperitoneal (IP) injection daily for 5 consecutive days. To activate CRE^{ER-T2} in *Lgr5$^{GFP-Cre}$;R26R^{tdTomato}* mice, we administered 2 mg tamoxifen IP on days 1 and 2. To delete floxed *Rbpj*, *Ascl2* and/or *Apc* alleles, we injected 2 mg tamoxifen IP on the 1st and 2nd days and 1 mg tamoxifen on the 3rd day. *Lgr5$^{GFP-Cre}$; R26R^{tdTomato}* and *Ascl2$^{Fl/Fl}$;Lgr5$^{GFP-Cre}$* mice received 10 Gy whole body γ-irradiation (^{137}Cs source) 96 h or 48 h, respectively, after the first dose of tamoxifen. To ablate ISCs in *Lgr5$^{Dtr-GFP}$* mice, we administered Diphtheria toxin (Sigma-Aldrich, 50 μg/kg) by IP injection 4 times on alternate days.

Detection of fluorescent cells in tissues

To detect *mCh$^+$*, *GFP$^+$*, and *tdTomato$^+$* cells, we fixed mouse small and large intestines in 4% paraformaldehyde (PFA) in phosphate-buffered saline (PBS) at 4°C overnight with gentle agitation, washed the specimens 3 times in PBS at 4°C, and rotated them overnight at 4°C in 30% sucrose in PBS. Tissues were embedded in OCT compound (Tissue-Tek, 4583) and stored at −80°C. Tissue sections (8 μm) adhered onto glass slides were washed in PBS and mounted in medium containing 4′,6-diamidino-2-phenyl-indole (DAPI – Vector Laboratories, H-1200). Fluorescent cells were visualized and counted using a spinning disc confocal microscope (Yokogawa). Images were analyzed by Fiji software (Schindelin et al., 2012). In experiments with *GFP$^+$Tomato$^+$* cells, *GFP$^+$* cells were counted first and then examined for *Tomato$^+$* in the red channel to determine if they were double positive.

Immunofluorescence

Intestinal or gastric tissue sections (5-7 μm thick) were incubated overnight with CLU (R&D Systems Inc, AF2747, 1:40), phospho-STAT3 (Cell Signaling, 9145, 1:100) or cleaved Caspase-3 (Cell Signaling, 9664, 1:100) antibodies (Ab) at 4°C, followed by Alexa Fluor 488- or Alexa Fluor 594-conjugated anti-mouse (Invitrogen, A-21202, 1:2,000) or anti-rabbit IgG (Invitrogen, A-11034 or A-11037, 1:2000) for 1 h at room temperature. To determine fractions of IL11RA$^+$ mCh$^+$ cells, we mixed IL11RA antibody (R&D

Systems, AF490) with Alexa Fluor 488-conjugated anti-goat IgG (Invitrogen, A-11055) on ice for 1 h and incubated with crypt single-cell suspensions for 30 min on ice. Cells were washed 5 times with cold PBS and analyzed on a Sony SH800z flow cytometer.

Colonic cell isolation

Immediately after euthanasia of mice by CO_2 inhalation, the proximal colon was harvested and ~2-mm slices were cut with a razor blade. These slices were washed briefly in in, then rotated in 10 mM EDTA solution prepared in Dulbecco's Modified Eagle/F-12 medium (DMEM/F-12, Life Technologies, 12634010) conditioned by growth of Wnt3a (70%) and Rspo1 (30%) secreting cells for 30 min at room temperature with change of solution every 10 min. Wnt3a was generated from L-Wnt-3A cells (ATCC, CRL-2647) and Rspo1 from HA-R-Spondin1-Fc293T cells (Ootani et al., 2009). Crypt epithelium released by this treatment was washed in DMEM (Corning, 17-205-CV), then digested for 30 min at 37°C in a mixture of 2.5 mL Accumax (Innovative Cell Technologies, AM105), 2.5 mL Dispase (Stem Cell Technologies, 07913), 0.5 mL TrypLE (Thermo Fisher, A1217702), 1.5 mL Wnt3a- and 0.5 mL Rspo1- conditioned media, washed in PBS, and passed through 35 μm filters (Falcon, 352235) to prepare single-cell suspensions. Live mCh$^+$ or GFP$^+$ cells were sorted on a Sony SH800z flow cytometer, using far-red dye (Life Technologies, L10120) or SYTOX Blue (Life Technologies, S34857) to exclude dead cells. Data were analyzed using FlowJo software (BD Biosciences).

Culture and analysis of colonic organoids

Single colonic epithelial cells isolated by flow cytometry were cultured as described (Sato et al., 2009) in Matrigel droplets (BD Biosciences, 356231) supplemented with 1 μM Jagged-1 peptide (AnaSpec, 61298) and covered with 0.5 mL Wnt3a (70%) and R-spo1 (30%) conditioned medium supplemented with antibiotics, N-2 and B-27 supplements and rEGF as described (Sato et al., 2009). In various experiments, 10 μg/ml NOV (R&D Systems, 1976-NV-050), 10 ng/ml FGF18 (R&D Systems, 8988-F18-050), or IL-11 (Peprotech, 220-11, 0.1 μg, 0.2 μg or 0.4 μg) was added to the culture medium. Each image in Figures 5D, 7E, and S7B is a composite of multiple overlaid photomicrographs. For passaging, organoids were disaggregated manually by pipetting, then transferred to fresh Matrigel droplets for further culture as above. Organoids were visualized using a Celigo S Imaging Cytometer (Nexcelom) to capture at least 5 focal planes, then counted on the resulting images, ensuring that each structure was counted only once. For histology, organoids were fixed for 15 min in 4% PFA in PBS at room temperature, while still in Matrigel, then incubated in 5 U Dispase (Stem Cell Technologies, 07913) at 37°C for 30 min to remove Matrigel, and fixed overnight at 4°C in 4% PFA in PBS. Organoids were then embedded in OCT compound (Tissue-Tek, 4583), frozen at −80°C, and 8 μm sections were cut for staining with hematoxylin and eosin.

RNA isolation and sequencing

For studies on bulk cell populations, mCh$^+$ or GFP$^+$ cells were isolated by flow cytometry (Sony SH800z Cell Sorter) directly into Trizol reagent (ThermoFisher, 15596026). RNA was purified as recommended by the manufacturer, treated with Turbo DNase I (Life Technologies, AM1907) to eliminate DNA contaminants, and purified over RNeasy columns (QIAGEN, 74104). Total RNA (5 to 10 ng) was used to prepare libraries with SMARTer Universal Low Input RNA kits (Takara Bio, 634940). Libraries were sequenced on a NextSeq 500 instrument (Illumina) to obtain 75-bp single-end reads. For scRNA-seq, we purified mCh$^+$ (Ascl2$^+$) 'upper' cells from mouse colons 8 days after ISC ablation, using flow cytometry. About 10^4 cells were loaded onto Chromium Chip B using the 3′ GEM Library & Gel Bead Kit v3 (10X Genomics), followed by reverse transcription, cDNA amplification, and library preparation according to the manufacturer's recommendations. Libraries were sequenced on a HiSeq4000 instrument (Illumina).

Chromatin immunoprecipitation (ChIP-seq)

ChIP for FLAG-tagged ASCL2 on the typically small number of resting or regenerating ISCs (< 20,000 colonic ISCs or mCh$^+$ 'upper' cells from *Ascl2^{Dfci}* mice) required special methods, including Tn5 transposition to isolate bound fragments. As a negative control, we performed ChIP on an equal number of GFP$^+$ colonic ISCs (no FLAG epitope, from *Lgr5$^{Dtr-GFP}$* mice). Cells were fixed in 1% formaldehyde in PBS for 10 min, followed by quenching with 0.125 M Glycine for 10 min, both at room temperature. Fixed cells were washed in cold lysis buffer (10 mM Tris HCl pH 7.4, 10 mM NaCl, 3 mM $MgCl_2$, 0.1% (v/v) Igepal CA-630) and incubated for 30 min on ice in ATAC-RSB^{2+} buffer (10 mM Tris Hcl pH 7.4, 10 mM NaCl, 3 mM $MgCl_2$, 0.1% Igepal CA-630, 0.1% Tween-20, 0.01% Digitonin) (Corces et al., 2017). Cells were then washed twice in cold lysis buffer and incubated with Tn5 in 50 μL Transposition mix (Illumina, FC-121-1030) for 30 min at 37°C with agitation at 1,000 RPM (Thermomixer, Eppendorf). Reactions were stopped by adding 150 μL SDS buffer (50 mM Tris HCl pH 8, 10 mM EDTA, 1.35% SDS) on ice for 1 h. SDS was then diluted by adding 750 μL 2xChIP buffer (100 mM Tris HCl pH 8, 0.3 M NaCl, 2 mM EDTA, 1mM EGTA, 1% N-lauroylsarcosine, 2% Triton X-100) and 550 μL water. After rotation for 2 h at 4°C, cell debris were removed by centrifugation and 5 μg FLAG antibody M2 (Sigma-Aldrich, F1804) was added to the supernatant, with overnight rotation at 4°C. Antibody-associated chromatin was isolated with Protein G Dynabeads (Thermo Fisher, Q32854, 50 μL) for 4 h at 4°C, washed twice each with RIPA-LS (10 mM Tris HCl pH 8, 140 mM NaCl, 1 mM EDTA, 0.1% SDS, 0.1% Na-Deoxycholate, 1% Triton X-100), RIPA-HS (10 mM Tris HCl pH 8, 500 mM NaCl, 1 mM EDTA pH, 0.1% SDS, 0.1% Na-Deoxycholate, 1% Triton X-100), RIPA-LiCl (10 mM Tris HCl pH 8, 250 mM LiCl, 1 mM EDTA, 0.1% Na-Deoxycholate, 0.5% Igepal CA-630), and TE buffer (10 mM Tris pH 8, 1 mM EDTA).

Immunoprecipitated chromatin was eluted in 100 μL elution buffer (50 mM Tris HCl pH 8, 10 mM EDTA, 1% SDS) and cross-links were reversed overnight at 65°C, followed by treatment with 0.2 mg/mL RNase A in 100 μL TE buffer for 2 h at 37°C and with 0.2 mg/mL Proteinase K and 300 mM $CaCl_2$ for 1 h at 37°C. DNA was extracted and precipitated with phenol, chloroform, isopropanol, Na

acetate, and linear acrylamide as a carrier. DNA was washed with 70% ethanol, resuspended in water, amplified over 16 cycles using high-fidelity 2X PCR Master Mix, and purified over columns (QIAGEN, 28004). After removal of primer dimers (< 100 bp) using AMPure beads (Beckman Coulter, A63881), the libraries were sequenced on a NextSeq 500 instrument (Illumina) to obtain 75-bp single-end reads.

QUANTIFICATION AND STATISTICAL ANALYSIS

General

For reproducible quantitation of crypts with GFP$^+$tdTom$^+$ or GFP$^+$tdTomato$^-$ cells, we assessed 5 independent wild-type intestines (Figures 1C and 3A), 5 $Ascl2^{-/-}$ intestines at 112 days and 2 $Ascl2^{-/-}$ intestines at 28 days (Figure 3A). Bar graphs in these panels represent mean ± SD of crypts containing GFP$^+$ ISCs. To examine ISC maintenance and restoration, crypts with GFP$^+$ cells were counted in every microscopic field from 6 (Figure 1E), 4 (Figure 1F), 5 (Figures 2D and 5B and 8 days) or 3 (Figure 5B, 10 days) independent control and experimental (each) animals. All samples were inspected randomly and, when feasible, blindly. Within the dot plots (Figures 1E, 1F, 2D, and 4B), boxes demarcate quartiles 1 and 3, bars represent median values, whiskers represent 1.5 times the inter-quartile range, and differences were assessed using Student's t test. We assessed post-irradiation lifespans in 5 independent $Ascl2^{-/-}$ and equal numbers of control mice (Figure 4A), using the log-rank test in GraphPad Prism 7 to generate survival curves. ISC positions in colonic crypts were assessed in 4 independent mice (Figure 2A) and 5 or 3 independent animals treated with DT for 8 or 10 days, respectively (Figure 5B). Organoid cultures from single crypt cells were generated from a minimum of 3 mice for each condition (Figures 5D, 7E, and S7B). Relative organoid numbers are expressed in relation to those that cells yielded in the corresponding control conditions; differences were evaluated by Student's t test and error bars in graphs that depict relative organoid numbers (ratios) represent SDs. IL11RA expression was examined by flow cytometry in cells isolated from N = 3 independent mice of each genotype.

Computational analyses

Raw reads from RNA- and ChIP-seq were aligned to the mouse genome (Mm10, Genome Reference Consortium GRCm38) using STAR aligner v2.53a (Dobin et al., 2013) for RNA or Bowtie2 (Langmead and Salzberg, 2012) for ChIP data. RNA-seq data quality was assessed using VIPER (Cornwell et al., 2018) and transcript levels were expressed as read counts using HTSeq (Anders et al., 2015). Sex chromosome-encoded and ribosomal genes were removed for comparative analyses. Data were normalized, and sample variability assessed by principal component analysis in DEseq2 (Love et al., 2014). Expression values were represented as reads per kilobase per million sequence tags (RPKM) and differential expression was defined in DEseq2 using the indicated Log$_2$ fold-changes, false discovery rates (FDRs) and basemeans. Volcano plots of differentially expressed RNAs were generated using the ggplot2 package in R (Wickham, 2009).

For ChIP-seq, we used MACS (Zhang et al., 2008) to align signals in raw (bam) files, then filtered to remove PCR duplicates and reads that aligned to multiple locations. Signals across samples were quantile normalized with Haystack (Pinello et al., 2014), using 50-bp windows across the genome. Sites bound to FLAG-ASCL2 in regenerating colonic crypt cells (enriched over the background in resting FLAG-negative $Lgr5^{Dtr-Egfp}$ ISCs) were identified using diffReps (Shen et al., 2013), with z-score cut-off 5, window size 200 bp, step size 20, and p value 0.0001. Raw signals from individual samples of a given cell type were converted to signal files (bigWig) using deepTools v2.1.0 (Ramírez et al., 2016). To impute candidate ASCL2 targets (Figure 7A), we considered genes differentially expressed between resting ISCs and mCh$^+$ 'upper' cells ($q < 10^{-5}$, 2X change, n = 316) and differential promoter ChIP-seq signals in regenerating cells compared to resting ISCs. RNA and ChIP signals at individual loci were visualized using the Integrated Genomics Viewer v2.3 (Robinson et al., 2011).

Single-cell RNA-seq

A library with 190,971,192 raw reads was aligned to the GRCm38/mm10 mouse genome, and Cell Ranger v3.0.2 (10X Genomics) was used to estimate unique molecular identifiers (UMIs). Raw aligned features were loaded and processed using the Seurat v3.0.2 package (Butler et al., 2018) in R version 3.6.1 (R Core Team, 2013). We retained only cells with ≥ 4,000 UMIs, ≥ 1,200 unique genes, < 20% mitochondrial gene contribution, and expression novelty (log$_{10}$ Genes per UMI) > 0.8 (Figure S5D). These 3,254 cells gave information on 14,737 genes.

Normalization, reduction of dimensionality, and clustering

Data were normalized in Seurat and variable genes were detected using Variance Stabilization transformation, followed by scaling and principal component (PC) analysis. The top 10 PCs were used to construct a Shared Nearest Neighbor graph and determine cell clusters, followed by reduction of dimensionality using the Uniform Manifold Approximation and Projection (UMAP) technique (McInnes et al., arXiv:1802.03426. Clusters co-expressing ISC (e.g., $Cdca7$) and colonocyte (e.g., $Fabp2$) or goblet cell (e.g., $Muc2$) markers were designated as transitional cells (Figure 6C), while clusters with high lone expression of ISC or lineage markers were designated accordingly. Total normalized counts for groups of known marker genes were used to determine cell cycle progression ($Plk1$, $Rrm2$, $Ccna2$, $Ccnb1$, $Ccnb2$, $Cdk1$, $Cdc25c$, $Cdca2$, $Cdc20$, $Ccne2$, $Cdc6$, $Cdc45$) or inhibition ($Cdkn2b$, $Cdkn2a$, $Cdkn1a$, $Cdkn1c$) (Figure 6B).Normalized count data were used to determine relative expression levels of genes in defined cell populations (Figure 6C – violin plots generated using the ggplot2 package in R).

Pseudotime analysis (Figure 6D)

Filtered data from Seurat were modeled in Monocle v2.12.0 (Trapnell et al., 2014) using the negative binomial distribution. After calculating size factors and dispersion using default parameters, differential genes were detected in the above-defined cell types using Seurat (cut-off $q < 0.01$). Dimensionality reduction and trajectory reconstruction were done within Monocle using the advanced nonlinear reconstruction algorithm DDRTree to determine two components (Mao et al., 2015). The branch of the trajectory plot with the most ISCs was used as the end-state to determine pseudotime for all cells, then dedifferentiation dynamics of cell groups were analyzed using pseudotime and lineage marker expression.

Mathematical modeling to quantify relative fitness of $Ascl2^{-/-}$ ISCs

We adapted a simple mathematical model of ISC dynamics (Lopez-Garcia et al., 2010), based on a Moran model on the cycle graph with a fixed number (N) of ISCs arranged in a ring (Figure 3D). M is the initial number of $Ascl2$-recombined (mutant, tdTom$^+$) ISCs and the remaining cells, $N-M$, escaped recombination (tdTom$^-$). Cells are placed uniformly at random on the cycle graph, so that each initial configuration is equally likely. We sampled an exponential waiting time for each ISC (i.e., each vertex in the graph), with rates λ_{WT} and λ_{Mut} for WT and mutant ISCs, respectively (each defined to 2 decimal places), and the smallest waiting time determines which cell divides first. One daughter then takes the parent's spot and the other replaces one or the other flanking ISC, each with probability 0.5. We updated the configuration of cells and repeated this process until fixation, i.e., when all ISCs were tdTom$^+$ or tdTom$^-$. Because 2D tissue sections miss infrequent tdTom$^-$ ISCs (which must be there), we considered tdTom$^+$ crypts to be 'predominantly' tdTom$^+$, making predominance precise as a parameter of the model.

We implemented exact stochastic simulations of this process over a range of parameter regimes, fixing N between 10 and 14 (Snippert et al., 2010) for each regime; replacing this number with a distribution did not change the results significantly. We also explored a range of values for M, fixing it deterministically or sampling it according to various plausible distributions, and set λ_{WT} to 0.25 and 0.5 divisions/day in the colon and duodenum, respectively (Snippert et al., 2014). We then estimated λ_{Mut} by optimizing over λ_{Mut} values to fit the model to the data. Each set of parameters produced a plot of the form shown in Figures S3A and S3B. At the start, all crypts are predominantly tdTom$^+$ (mutant) and the point trajectories show that fraction decreasing over time as wild-type ISCs gradually exert their advantage. The lines eventually flatten and converge as crypts fixate as predominantly tdTom$^+$ or tdTom$^-$. Raising mutant fitness would pull all point trajectories upward, so the optimization procedure amounts to identifying the λ_{Mut} value that minimizes the squared difference between predicted and observed results, for a fixed set of plausible parameters. We obtained an estimate for $Ascl2^{-/-}$ ISC disadvantage for each regime (examples in Figure S3C).

DATA AND CODE AVAILABILITY

All RNA, ChIP, and ATAC data are deposited in the Gene Expression Omnibus (GEO). The accession number for these data is GEO: GSE130822. No previously unpublished custom code was used to analyze the data.